



Multiwavelength Study of a Hyperluminous X-Ray Source near NGC 6099: A Strong IMBH Candidate

Yi-Chi Chang¹ , Roberto Soria^{2,3,4} , Albert K. H. Kong¹ , Alister W. Graham⁵ , Kirill A. Grishin^{6,7} , and Igor V. Chilingarian^{8,7}

¹ Institute of Astronomy, National Tsing Hua University, Hsinchu 30013, Taiwan; judy.chang@gapp.nthu.edu.tw, akong@gapp.nthu.edu.tw

² INAF-Osservatorio Astrofisico di Torino, Strada Osservatorio 20, I-10025 Pino Torinese, Italy

³ Sydney Institute for Astronomy, School of Physics A28, The University of Sydney, Sydney, NSW 2006, Australia

⁴ College of Astronomy and Space Sciences, University of the Chinese Academy of Sciences, Beijing 100049, People's Republic of China

⁵ Centre for Astrophysics and Supercomputing, Swinburne University of Technology, Hawthorn, VIC 3122, Australia

⁶ Universite Paris Cité, CNRS, Astroparticule et Cosmologie, F-75013 Paris, France

⁷ Sternberg Astronomical Institute, M.V. Lomonosov Moscow State University, Universitetsky pr., 13, 119234, Moscow, Russia

⁸ Center for Astrophysics—Harvard & Smithsonian, Cambridge, MA 02138, USA

Received 2024 August 6; revised 2025 February 24; accepted 2025 February 27; published 2025 April 11

Abstract

We report on the intriguing properties of a variable X-ray source projected at the outskirts of the elliptical galaxy NGC 6099 ($d \approx 139$ Mpc). If truly located near NGC 6099, this is a hyperluminous X-ray source that reached an X-ray luminosity $L_X \approx$ a few times 10^{42} erg s^{-1} in 2012 February (XMM-Newton data), about 50–100 times brighter than in 2009 May (Chandra) and 2023 August (XMM-Newton). The X-ray spectrum was soft at all three epochs, with a thermal component at $kT \approx 0.2$ keV and a power-law photon index >3 . Such properties make it a strong candidate for an intermediate-mass black hole (IMBH). We also discovered a point-like, blue optical counterpart ($m_{g,\text{Vega}} \approx 24.7$ mag, $M_{g,\text{Vega}} \approx -11.2$ mag), from images taken by the Canada–France–Hawaii Telescope and later confirmed with Hubble Space Telescope observations. The optical continuum can be modeled as stellar emission from a compact star cluster or an X-ray-irradiated accretion disk, consistent with the IMBH scenario. We discuss alternative explanations for the nature of this system. A possible scenario is tidal stripping of an orbiting star, with repeated X-ray outbursts every few years. An alternative possibility is that the thermal X-ray emission seen in 2009 was from shocked gas in the self-intersecting tidal stream during the rising phase of a tidal disruption event, while the 2012 and 2023 emissions were from the fully formed accretion disk.

Unified Astronomy Thesaurus concepts: [Accretion \(14\)](#); [Intermediate-mass black holes \(816\)](#); [X-ray binary stars \(1811\)](#); [Ultraluminous x-ray sources \(2164\)](#)

1. Introduction

The existence of intermediate-mass black holes (IMBHs; F. Koliopoulos 2017; J. E. Greene et al. 2020; M. Volonteri et al. 2021) in the mass range $\sim 10^3$ – $10^4 M_\odot$ is favored by theoretical arguments, such as their role as seeds for the rapid growth of supermassive black holes (SMBHs; M. Volonteri et al. 2008; A. Ricarte & P. Natarajan 2018; K. Inayoshi et al. 2020; R. L. Larson et al. 2023), with masses $> 10^9 M_\odot$ already at $z \gtrsim 6$ (D. J. Mortlock et al. 2011; E. Bañados et al. 2018; J. Yang et al. 2020; F. Wang et al. 2021; X. Fan et al. 2023). Some of the unanswered questions are how many IMBHs have survived in the present-day Universe, where are they located, and how can we observe them (M. Mezucia 2017; R. S. Barrons et al. 2024)?

Three possible local-Universe environments where IMBHs may exist are: (i) in the cores of massive globular clusters, where they may have been formed from the rapid core collapse and runaway mergers of O stars (M. C. Miller & D. P. Hamilton 2002; S. F. Portegies Zwart & S. L. W. McMillan 2002; M. A. Gürkan et al. 2004; M. Freitag et al. 2006; U. N. Di Carlo et al. 2021); (ii) in the nuclei of dwarf galaxies and late-type disk galaxies, if the scaling relations between spheroidal

stellar mass and nuclear black hole (BH) mass can be extrapolated to such a mass range (A. W. Graham 2016, 2023; I. V. Chilingarian et al. 2018; B. L. Davis & A. W. Graham 2021; A. W. Graham et al. 2021); and (iii) floating in the halos of massive galaxies (“wandering IMBHs”: J. M. Bellovary et al. 2010; J. E. Greene et al. 2021; B. S. Seepaul et al. 2022; T. Di Matteo et al. 2023), perhaps still inside a tightly bound stellar cluster, as a result of gravitational recoil and/or tidal stripping of accreted and disrupted satellite dwarfs.

In this work, we report on the X-ray spectral and timing properties of an IMBH candidate in the local Universe: 2CXO J161534.2+192707 (I. N. Evans et al. 2010, 2024) = 4XMM J161534.3+192707 (N. A. Webb et al. 2020; H. Tranin et al. 2022). This source is located in projection in the halo of the elliptical galaxy NGC 6099 ($d \approx 139$ Mpc). If it is at the same distance as the galaxy, its X-ray luminosity would have been $L_X \approx 4 \times 10^{42}$ erg s^{-1} in 2012. We also discovered and investigated its point-like optical counterpart, seen at $m_{g,\text{Vega}} \approx 24.7$ mag in 2022–2023. In Section 2, we describe the general reasons why we consider this source a strong off-nuclear IMBH candidate in the nearby Universe, and we discuss its spatial association with the nearby galaxy. In Section 3, we summarize the X-ray and optical observations used in this study and our data analysis techniques. In Section 4, we discuss the positional association of the X-ray source with a point-like optical counterpart. In Section 5, we report on the brightness and colors of the optical

counterpart. In Section 6, we model the X-ray spectral properties of the source in the 2009 Chandra observation (lower state), the 2012 XMM-Newton observation (higher state), and the 2023 XMM-Newton observation (lower state again). In Section 7, we combine the optical and X-ray data and model the broadband spectral energy distribution (SED); we illustrate the case of an irradiated accretion disk and of a star cluster. In Section 8, we summarize the multiband results and discuss possible interpretations for the source and its X-ray flux evolution.

2. X-Ray Search for IMBH Candidates

2.1. General Selection Criteria

Our focus is on IMBHs that are (or briefly become) X-ray active because of gas accretion and that are not spatially coincident with the nucleus of a major galaxy. Unfortunately, it is generally hard to distinguish between an off-nuclear X-ray-bright IMBH, a stellar-mass X-ray binary, and a background active galactic nucleus (AGN) that only happens to be seen in projection behind a nearby galaxy (e.g., I. Zolotukhin et al. 2016; H. P. Earnshaw et al. 2019; R. S. Barrows et al. 2024).

Our first selection criterion for a point-like, non-nuclear X-ray source to be considered an IMBH candidate is that it is probably too luminous to be a stellar-mass compact object at the distance of its apparent host galaxy. Stellar-mass BHs and neutron stars can reach apparent luminosities of several times 10^{40} erg s⁻¹, at highly super-Eddington accretion rates and with the help of moderate polar funnel beaming (ultraluminous X-ray sources or ULXs: H. Feng & R. Soria 2011; P. Kaaret et al. 2017; A. King et al. 2023). Thus, a somewhat conventional threshold to screen out stellar-mass accretors is an apparent isotropic 0.3–10 keV luminosity of 10^{41} erg s⁻¹: sources above this limit are usually referred to as hyperluminous X-ray sources (HLXs; Y. Gao et al. 2003; A. R. King & W. Dehnen 2005; A. D. Sutton et al. 2012; R. S. Barrows et al. 2019; A. D. A. MacKenzie et al. 2023; H. Tranin et al. 2024).

An apparent spatial association with a nearby galaxy does not guarantee that an X-ray source is really at the same distance as the galaxy: in the absence of redshift information on its optical counterparts, it may also be a background AGN randomly projected behind the galaxy (N. Masetti et al. 2003; M. Heida et al. 2013; A. D. Sutton et al. 2015; H. P. Earnshaw et al. 2019). To reduce the effect of this contamination, we searched for HLXs in the thermal dominant (“high/soft”) state (T. J. Maccarone et al. 2003; R. P. Fender et al. 2004; R. A. Remillard & J. E. McClintock 2006), which is at a dimensionless accretion rate $0.02 \lesssim \dot{m} \lesssim 1$, where $\dot{m} \equiv \dot{M}/\dot{M}_{\text{Edd}}$ and \dot{M}_{Edd} is the Eddington accretion rate, with $\dot{M}_{\text{Edd}} \equiv L_{\text{Edd}}/0.1c^2$, where L_{Edd} is the Eddington luminosity. We assume that the high/soft state of an accreting IMBH behaves like that of a stellar-mass BH, dominated by a standard Shakura–Sunyaev multicolor disk spectrum (N. I. Shakura & R. A. Sunyaev 1973; A. Merloni et al. 2000), with peak color temperature $kT_{\text{in}} \approx 230(\dot{m}/M_4)^{1/4}$ eV (N. I. Shakura & R. A. Sunyaev 1973; A. Kubota et al. 1998; C. Done et al. 2012), where M_4 is the BH mass in units of $10^4 M_{\odot}$. Therefore, point-like X-ray sources with apparent luminosities $\sim 10^{41}$ – 10^{43} erg s⁻¹, a soft thermal spectrum, and peak disk blackbody temperatures $kT_{\text{in}} \approx 0.2$ – 0.3 keV are strong IMBH candidates. The vast majority of background AGNs (powered by SMBHs) have a more dominant power-law component

above 1 keV, with characteristic photon indices ≈ 1.0 – 2.5 (E. Piconcelli et al. 2005; M. J. Page et al. 2006; A. Corral et al. 2011; S. Marchesi et al. 2016; D. Kynoch et al. 2023; M. Elías-Chávez et al. 2024), plus a fainter thermal component (“soft excess”) with characteristic temperatures $kT \approx 50$ – 150 eV (J. Crummy et al. 2006; C. Done et al. 2012), cooler than expected from an IMBH.

A further IMBH selection criterion is an X-ray flux variability of at least an order of magnitude between separate epochs observed by either Chandra or XMM-Newton. This is because an off-nuclear IMBH is unlikely to accrete from a steady galaxy-scale gas inflow or to receive a steady Roche-lobe mass transfer from a much less massive donor star. Either in the case of accretion from an individual donor star (V. Kalogera et al. 2004) or in the case of feeding from a tidal disruption event (TDE; N. C. Stone & B. D. Metzger 2016; D. Lin et al. 2018; R. Saxton et al. 2020), we expect transient X-ray outbursts.

Finally, an X-ray over the optical flux ratio $F_{\text{X}}/F_{\text{opt}} \gtrsim 10$ provides additional support for the IMBH classification. Most AGNs have $0.1 \lesssim F_{\text{X}}/F_{\text{opt}} \lesssim 10$ (E. Lusso et al. 2010; F. Civano et al. 2012; M. Heida et al. 2013), because their emission from the accretion disk peaks in the UV band. Foreground Galactic stars have a soft X-ray spectrum but $F_{\text{X}}/F_{\text{opt}} \lesssim 10^{-3}$. In practice, it is often difficult to have simultaneous X-ray and optical coverage of a source, especially in the case of X-ray transients.

The criteria outlined above are not a silver bullet for IMBH detection. For example, a small fraction of AGNs (“supersoft AGNs”) have a thermal spectrum with temperatures as high as ~ 0.2 keV and almost no power-law component or a power law with photon index $\Gamma > 3$ (Y. Terashima et al. 2012; A. Sacchi et al. 2023), similar to the predicted spectrum of an IMBH in the high/soft state. Nuclear SMBHs that become active as a result of a TDE are transient and often have purely thermal X-ray emission (R. Saxton et al. 2020; S. Gezari 2021). Other AGNs, known as changing-look or changing-state AGNs (S. Komossa & D. Grupe 2023), show X-ray luminosity variations by up to 2 orders of magnitude over a few years, sometimes also accompanied by a soft, thermal X-ray spectrum (M. Masterson et al. 2022). Moreover, at least one confirmed stellar-mass accretor, the ULX pulsar in NGC 5907, has approached an X-ray luminosity $\approx 10^{41}$ erg s⁻¹ (F. Fürst et al. 2017; G. L. Israel et al. 2017). Nonetheless, searching for soft X-ray transients in the outskirts of early-type galaxies, at $L_{\text{X}} \sim 10^{41}$ – 10^{43} erg s⁻¹, does provide a useful first screening of IMBH candidates for detailed follow-up investigations.

We applied the selection criteria described above to the XMM-Newton sources in the catalog of H. Tranin et al. (2022). Specifically, we selected sources with: (i) a luminosity $L_{\text{X}} > 10^{41}$ erg s⁻¹ if located in the apparent host galaxy; (ii) a luminosity distance of the presumed host galaxy < 300 Mpc; (iii) a photon index of the best power-law spectral fit $\Gamma > 3.0$; (iv) EPIC-pn hardness ratios⁹ HR3 < -0.5 and HR4 < -0.5 ; and (v) at least two observations between XMM-Newton, Chandra, and Swift with flux variations larger than 10 between different epochs.

⁹ The hardness ratio HR3 is defined as $(F3 - F2)/(F3 + F2)$, where $F3$ is the observed EPIC-pn flux in the 2.0–4.5 keV band and $F2$ is the flux in the 1.0–2.0 keV band. The hardness ratio HR4 is defined as $(F4 - F3)/(F4 + F3)$, where $F4$ is the 4.5–12.0 keV flux and $F3$ is the 2.0–4.5 keV flux. The softer a source is, the closer both those ratios are to -1 .

2.2. Our First Cut of Interesting Soft Sources

Out of about half a million sources in the H. Tranin et al. (2022) catalog, only seven sources satisfy the five selection criteria detailed above. We inspected and investigated each of these sources (using archival data and literature results) to check whether they did contain plausible IMBH candidates. One of the seven sources is an overdensity of hot gas in the nuclear region of the elliptical galaxy NGC 741 (N. N. Jetha et al. 2008; G. Schellenberger et al. 2017) and was therefore immediately dismissed. Two sources are well-known super-soft, strongly variable AGNs: the narrow-line Seyfert galaxies 1H 0707–495 = LEDA 88588 (T. Boller et al. 2002; T. Dauser et al. 2012; S. Hancock et al. 2023; A. Dobrotka et al. 2024; Y. Xu et al. 2024) and IRAS 13224–3809 = LEDA 88835 (J. Jiang et al. 2018, 2022; C. Pinto et al. 2018; W. N. Alston et al. 2019; M. D. Caballero-Garcia et al. 2020; S. Hancock et al. 2023; A. Dobrotka et al. 2024; Y. Xu et al. 2024). Both AGNs are of course extremely interesting objects for studies of ultrafast outflows, Compton reflection spectra, and disk flares, but they are not relevant to our search for off-nuclear IMBH candidates. A further source is associated to a close pair of merging galaxies at the outskirts of the galaxy cluster A1795: the LINER 2MASX J13482545+2624383 and the elliptical galaxy SDSS J134825.62+262435.7 (D. M. Nisbet & P. N. Best 2016; M. H. Abdullah et al. 2020). The large distance (≈ 280 Mpc) of A1795 makes it impossible to determine whether the soft XMM-Newton source corresponds to the nucleus of SDSS J134825.62+262435.7 or is slightly offset; an analysis of this system is left for further work.

This leaves three sources in our selected sample. One of them is ESO 243-49 HLX-1 (S. A. Farrell et al. 2009; R. Soria et al. 2017), projected in the halo of an S0 galaxy ($d \approx 95$ Mpc). This is perhaps the best-known off-nuclear IMBH candidate in the literature; it has shown repeated outbursts with state transitions and has a thermal disk blackbody spectrum at the peak of each outburst with a peak luminosity $L_X \approx 10^{42}$ erg s⁻¹. The second one is another well-known IMBH candidate, 3XMM J215022.4–055108 (D. Lin et al. 2018). This is a soft, thermal, transient source (probably triggered by a TDE) in a globular cluster at the outskirts of a lenticular galaxy ($d \approx 250$ Mpc). Its maximum observed luminosity is $L_X \approx 10^{43}$ erg s⁻¹, although it may have reached an even higher luminosity at the (unobserved) outburst peak. This leaves us with the last one of those seven soft, variable, X-ray sources: 2CXO J161534.2+192707 = 4XMM J161534.3+192707, near the elliptical galaxy NGC 6099 (Figure 1). Henceforth, we refer to this source as NGC 6099 HLX-1 or simply as HLX-1, for simplicity. It has received no special attention in the literature so far.¹⁰ We will show in this work that it is a strong IMBH candidate and that it has a point-like optical counterpart.

2.3. Our Best IMBH Candidate in the Halo of NGC 6099

NGC 6099 HLX-1 is projected inside the elliptical galaxy NGC 6099, $\approx 18''3$ west of its core. The r -band Petrosian radius (V. Petrosian 1976) of NGC 6099 is $14''6$

¹⁰ The same source 2CXO J161534.2+192707 is also listed in the ULX catalogs of K. Kovlakas et al. (2020) and M. C. I. Bernadich et al. (2022); however, the host galaxy identification and distance are wrong (it was mistakenly associated with a foreground star) and therefore it was not recognized as an HLX.

(R. Ahumada et al. 2020).¹¹ Two Petrosian radii can be taken as a conventional size to define the association of an X-ray source with a host galaxy (A. W. Graham & S. P. Driver 2005; I. Zolotukhin et al. 2016).

NGC 6099 has a spectroscopic redshift $z = 0.03043 \pm 0.00001$ (R. Ahumada et al. 2020), corresponding to a luminosity distance $d = (139 \pm 10)$ Mpc for the standard cosmological parameters adopted by the NASA/IPAC Extragalactic Database (NED; $H_0 = 67.8$ km s⁻¹ Mpc⁻¹, $\Omega_m = 0.308$, $\Omega_\Lambda = 0.692$). It has a gravitationally bound close companion with a similar size, morphology, and optical brightness, NGC 6098¹² (Figure 1), with a redshift $z = 0.03155 \pm 0.00001$ corresponding to a luminosity distance $d = (144 \pm 10)$ Mpc. It is likely that the discrepant redshift measured for the two elliptical galaxies corresponds to their relative proper motion (≈ 330 km s⁻¹)¹³ around their center of mass; in this case, the true luminosity distance of both galaxies may be intermediate between the two values given above. For this work, in the absence of any information on the proper motion of the two galaxies, we adopt the luminosity distance of 139 Mpc for NGC 6099 HLX-1, tied to the luminosity distance of its apparent host galaxy. At this distance, HLX-1 reached $L_X \sim$ a few 10^{42} erg s⁻¹ in one observation and varied in flux by a factor of at least 50 between observations (Figure 1).

3. Observations and Data Analysis

3.1. Chandra X-Ray Observatory (2009)

The field of NGC 6098/6099 was observed with the Advanced CCD Imaging Spectrometer (ACIS) on board NASA’s Chandra X-ray Observatory, on 2009 May 23, for a good time interval (GTI) of 44.6 ks (Table 1). We retrieved the observation files from the Chandra Data Archive and reprocessed them with the Chandra Interactive Analysis of Observations (CIAO), version 4.13 (A. Fruscione et al. 2006), with the Calibration Database, version 4.9.8. We created new level 2 event files with the CIAO task `chandra_repro`. We checked with `dmextract` that there were no significant background flares during the observation. We used `dmcopy` for energy filtering and to create images in different bands, and the imaging tool DS9 to display the images and define source and background regions. For the point-like source HLX-1, the source extraction region was a circle with a $2''$ radius; the background region was an annulus with an inner radius of $3''.5$ and an outer radius of $7''$. For the diffuse emission in the nuclei of the two elliptical galaxies, we used circular source regions with a radius of $4''$ for NGC 6099 and $5''$ for NGC 6098; the associated background regions were chosen to be at least four times the source extraction areas and not to include X-ray photons from HLX-1 or from other galaxies. We then used `specextract` to extract a spectrum and associated response and ancillary response files for HLX-1 (option `correctpsf = yes`) and for the extended emission in the nuclear regions (option `correctpsf = no`). The arcsec

¹¹ By comparison, the B -band D25 isophotal diameter listed in the NED (<https://ned.ipac.caltech.edu>) is $79''.1$, because it refers to the 25 mag isophote around the galaxy pair NGC 6098/99.

¹² Together, they form the galaxy pair KPG 493.

¹³ The relative motion of the two galaxies may be responsible for the ridge of soft, thermal, X-ray emission from shocked gas, ≈ 30 kpc to the southeast of the nucleus of NGC 6099, visible in both XMM-Newton and Chandra observations. An analysis of the properties of the shocked gas is beyond the scope of this paper.

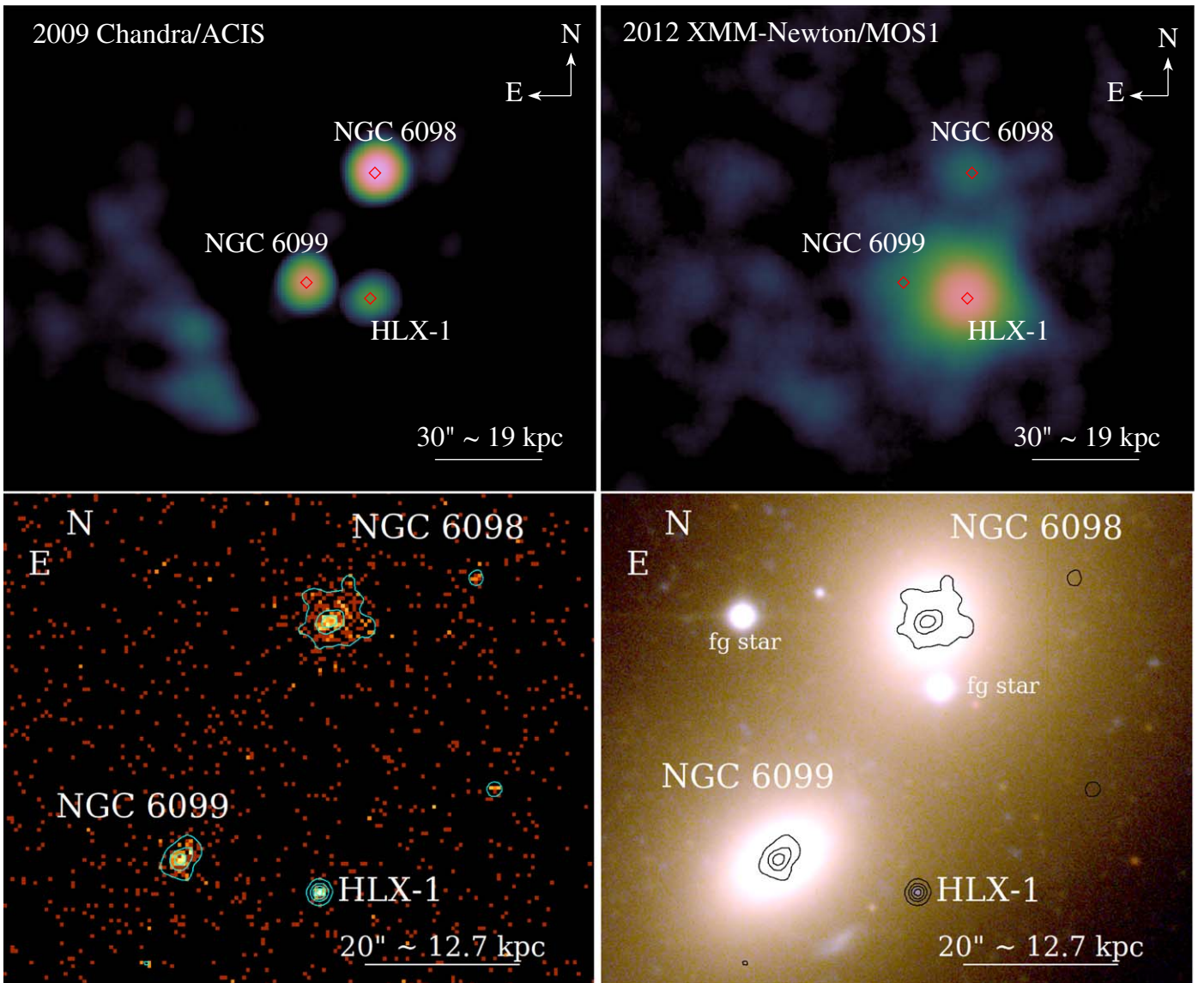


Figure 1. Top left: false-color, adaptively smoothed image from the 2009 Chandra/ACIS observation (0.3–8 keV band). Here, HLX-1 has an X-ray luminosity of a few $\times 10^{40}$ erg s^{-1} , slightly fainter than its two neighboring galaxies. A ridge of diffuse emission is also visible, ≈ 20 kpc southeast of NGC 6099. Top right: false-color, adaptively smoothed XMM-Newton/EPIC-MOS1 image (0.3–10 keV band) from 2012, displayed on the same spatial scale as the top left panel. At this epoch, HLX-1 vastly outshines the X-ray emission from NGC 6099 and NGC 6098. Bottom left: zoomed-in, unsmoothed 2009 Chandra/ACIS image (0.3–8 keV band), with smoothed X-ray flux contours overplotted in cyan (linear scale). Bottom right: true-color CFHT/Megacam image on the same scale as the bottom left panel, with Chandra/ACIS flux contours overplotted in black. The optical colors are blue = u band, green = g band, and red = r band. The bluish counterpart of HLX-1 stands out from the old-population halo of NGC 6099 and NGC 6098.

resolution of Chandra guarantees that there is no significant contamination of the ACIS spectrum of HLX-1 with diffuse thermal emission from NGC 6098 and NGC 6099 and vice versa (Figure 1).

For our spectral analysis, we used the FTOOLS (J. K. Blackburn 1995; NASA High Energy Astrophysics Science Archive Research Center (Heasarc) 2014) software suite, from NASA’s High Energy Astrophysics Science Archive Research Center (HEASARC). We rebinned the spectra to ≥ 1 count per bin with `grppha` and modeled them in the 0.3–8.0 keV band with the spectral analysis package XSPEC version 12.13.0c (K. A. Arnaud 1996). Because of the low number of counts (only ≈ 50 net counts for HLX-1), we used the `cstat` statistics (W. Cash 1979) for the fit statistics. Error ranges (90% confidence limit) for the fit parameters were calculated with the `steppar`, `error` task in XSPEC. Confidence limits for the

luminosity distances were calculated with the PYTHON package `uncertainties` version 3.1.7: <http://pythonhosted.org/uncertainties/>.

3.2. XMM-Newton (2012 and 2023)

The European Space Agency’s XMM-Newton space observatory observed the field of NGC 6098/6099 on two occasions: on 2012 February 25 (ObsID 0670350301, Rev. 2237; PI: John Mulchaey), with an exposure time of ≈ 16.6 ks, and on 2023 August 4 (ObsID 0923030101, Rev. 4332; PI: Albert Kong), for ≈ 88 ks. Henceforth, we will usually refer to these two data sets as XMM1 and XMM2, for shorthand notation. On both occasions, the European Photon Imaging Camera (EPIC) was the prime instrument, with two MOS and one pn detector.

Table 1

Log of the X-Ray Observations of the Field of NGC 6099 Analyzed in This Paper

Observ.	Detector	ObsID	Start Date	GTI (ks)
Chandra	ACIS	10230	2009 May 23	44.6
XMM1	MOS	0670350301	2012 Feb 25	14.5
	pn	0670350301	2012 Feb 25	10.6
Swift1	XRT	00014346001	2021 Jun 18	1.7
Swift2	XRT	00014346002	2021 Jun 20	0.9
Swift3	XRT	00097139001	2023 Apr 9	2.8
Swift4	XRT	00097139002	2023 Jun 28	1.8
Swift5	XRT	00097139003	2023 Jul 12	1.0
XMM2	MOS	0923030101	2023 Aug 4	85.2
	pn	0923030101	2023 Aug 4	69.7
Swift6	XRT	00097139004	2023 Oct 9	2.5
Swift7	XRT	00097139005	2024 Jan 9	2.8

We downloaded the data files from the XMM-Newton Science Archive; XMM1 was already in the public domain, while XMM2 was the result of a follow-up observation proposed by our team specifically for HLX-1—it is also now publicly available. We processed both data sets with the XMM-Newton Science Analysis System (SAS) v20.0.0 software, with the calibration files updated to 2021 November 13. We used the `eproc` and `emproc` tasks to reprocess the observation data files and obtain calibrated and concatenated event lists. To filter out intervals of flaring background, we set a rejection threshold of 0.35 ct s^{-1} for each MOS and 0.4 ct s^{-1} for the pn, over the full field of view at channel energies above 10 keV; the filtering was done with the SAS task `tabgtigen`. In XMM1, we retained a GTI of 14.5 ks for EPIC-MOS and 10.6 ks for EPIC-pn; in XMM2, the GTI was 85.2 ks for EPIC-MOS and 69.7 ks for EPIC-pn.

We used the SAS task `xmmselect` to define source and background extraction regions, and to build spectral files and associated response and ancillary response files, for each detector. Given the small angular separation between HLX-1 and the nucleus of NGC 6099 ($\approx 18''$, computed from the Chandra image), we need to assess and minimize the possible contamination of the HLX-1 spectrum from the diffuse hot-gas emission of the nearby galaxy. This means taking a source extraction region for HLX-1 large enough to include most of the source counts but not so large as to be significantly contaminated by the diffuse NGC 6099 emission. The latter can be assumed to be constant over human timescales. Its intensity was measured from the Chandra data (Section 6.1) and converted to the expected XMM-Newton/EPIC count rates with the Portable, Interactive Multi-Mission Simulator software, version 4.12d. Its spatial extent in Chandra/ACIS was then convolved with the point-spread function (PSF) of the XMM-Newton/EPIC detectors.

We find that in XMM1, the total diffuse NGC 6099 emission is insignificant compared with the emission from HLX-1 (Figure 2). For all three EPIC instruments of the XMM1 data set, we used a source extraction circle of $14''$ radius for HLX-1, and estimated that the contamination of the galactic hot-gas emission falling inside that circle is $<1\%$. For XMM2, the total diffuse NGC 6099 emission is slightly higher than the HLX-1 emission (Figure 3). Thus, we chose to reduce the HLX-1 source extraction circle to a radius of $10''$, to keep the contamination from diffuse galactic emission to $<1\%$ of the HLX-1 source emission. On the contrary, any possible

contamination from the diffuse emission in the other nearby elliptical galaxy, NGC 6098, is completely negligible both in 2012 and in 2023. For both the XMM1 and XMM2 data sets, we defined the composite background region as three circles, each with a radius of $20''$, within $\approx 1'$ of the HLX-1 position, taking care to avoid the nuclear emission from NGC 6098 and NGC 6099, the diffuse emission ridge southeast of NGC 6099, and any chip gaps.

With this choice of source and background regions, we extracted EPIC-pn light curves of HLX-1, with the standard tasks `xmmselect` and `epiclccorr`. We then extracted EPIC-MOS and EPIC-pn spectra and built the associated response and ancillary response files with `xmmselect`, `rmfgen`, and `arfgen`. For all light curves and spectra, we used a spectral bin size of 5 eV.

We rebinned the EPIC-pn and EPIC-MOS spectra to a minimum of 20 counts per bin with `grppha`, suitable for the χ^2 fitting statistics. For each observation data set, we modeled the three EPIC spectra, simultaneously with XSPEC. As a first step, we selected the energy range of 0.2–10 keV for the MOS detectors and 0.2–12 keV for the pn, for the 2012 and 2023 data sets. However, the 2023 images (Figure 3) and spectra show no significant net counts from HLX-1 above 5 keV and very few counts above 2 keV. Therefore, to limit the contamination from background photons, we ignored channels above 5 keV in the 2023 spectra. We used the χ^2 statistics for the computation of the best-fitting parameter values and 90% confidence intervals of the upper and lower bounds.

3.3. Swift X-Ray Observatory

The X-Ray Telescope (XRT) on board the Niels Gehrels Swift Observatory took seven snapshot observations of NGC 6099 between 2021 June 18 and 2024 January 9. The total effective (i.e., accounting for vignetting) exposure time at the location of HLX-1 was 12.3 ks. We retrieved the data from NASA’s HEASARC public archive and processed them with the Swift/XRT data analysis tools available online.¹⁴ X-ray emission from the nuclei of NGC 6098 and NGC 6099 is marginally detected in the stacked 0.3–10 keV image, but HLX-1 is not detected in any observation, nor in the stacked data set. We estimated the total observed counts in a $10''$ source extraction circle in the stacked image and the expected background counts in regions at a similar distance from the nucleus of NGC 6099. We then applied the statistics of R. P. Kraft et al. (1991) to determine the confidence interval for a source with a low number of counts. After taking into account the XRT aperture correction from $10''$ to infinity, we converted the 90% upper limit on the net source counts into a 90% upper limit on the observed flux, assuming the same spectral model fitted to the nearest XMM-Newton observations (XMM2). With this method, and correcting for line-of-sight absorption, we estimate a 90% upper limit to the luminosity of HLX-1 in the stacked Swift/XRT data set of $L_X = (5 \pm 1) \times 10^{40} \text{ erg s}^{-1}$, consistent with the XMM-Newton results from 2023 (Section 6.3).

3.4. Canada–France–Hawaii Telescope

We observed the field of NGC 6099 with the MegaPrime/MegaCam detector on the 3.6 m Canada–France–Hawaii Telescope (CFHT) on 2022 August 2 (OBSID 2773230). The

¹⁴ https://www.swift.ac.uk/user_objects/

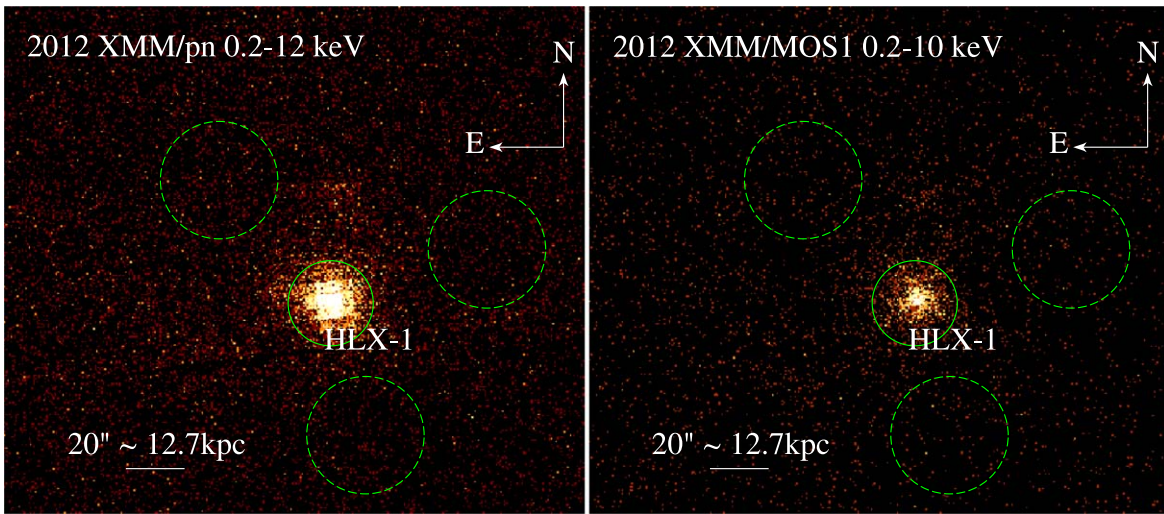


Figure 2. XMM-Newton/EPIC pn (left) and MOS1 (right) images from the 2012 observation. The solid green circles (radius of $14''/5$) define the source extraction regions for our timing and spectral analyses of HLX-1; the dashed circles (radii of $20''$) map the background regions. The contribution from the diffuse emission around the nuclei of NGC 6098 and NGC 6099 is negligible, compared with the emission from HLX-1.

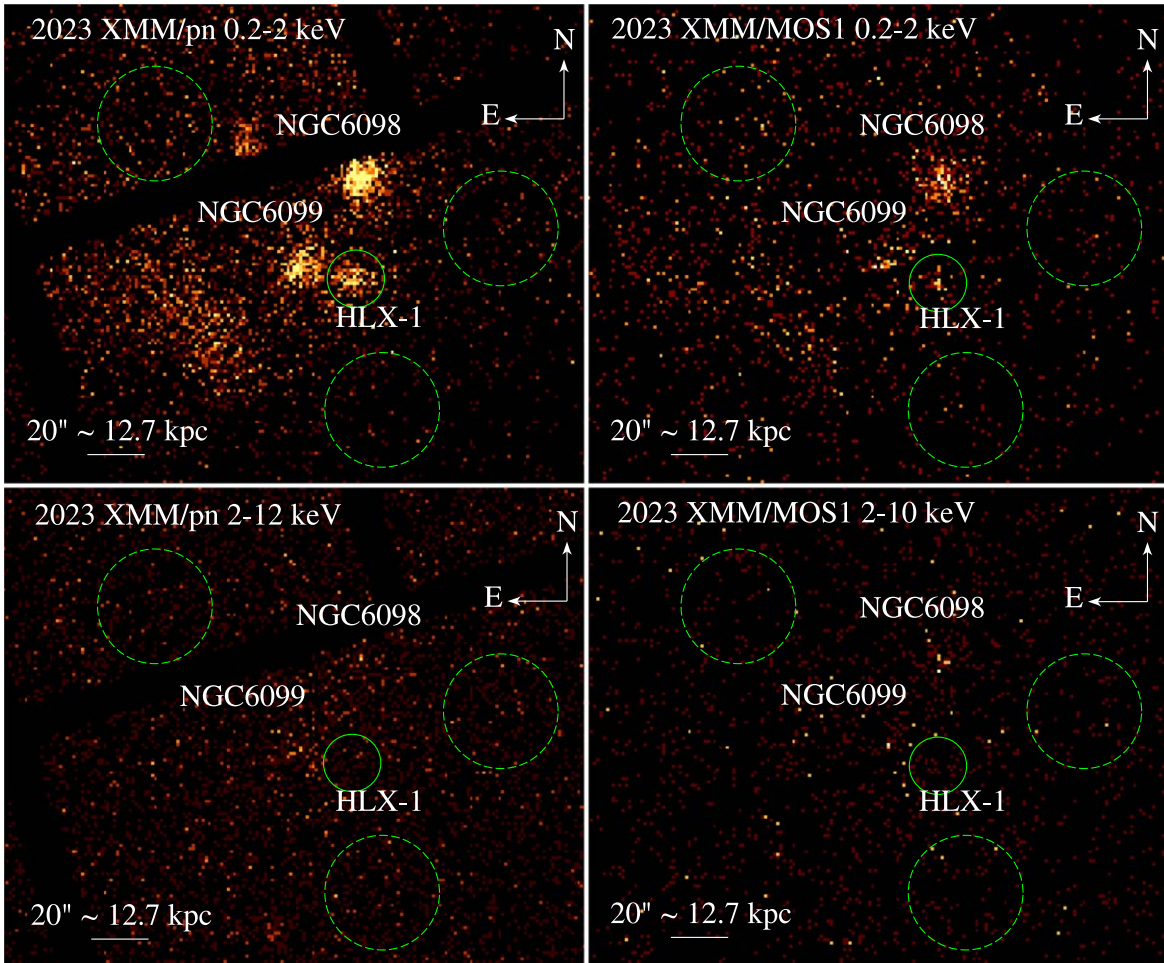


Figure 3. XMM-Newton/EPIC pn and MOS1 images from the 2023 observation, in different energy bands; the field of view is the same as in Figure 2. Top: soft band (0.2–2 keV); bottom: hard band (2–12 keV for pn, 2–10 keV for MOS1). In each panel, the solid green circle (radius of $10''$) is the source extraction region for HLX-1, and the dashed green circles (radius of $20''$) map the background regions. These images show that the 2023 flux of HLX-1 has declined below the flux of the diffuse emission from NGC 6099; it also highlights the softness of its spectrum.

images cover a $1^\circ \times 1^\circ$ field of view, with a resolution of $0''.187$ per pixel. We took four images in the u band (u.MP9302 filter), two in the g band (u.MP9402 filter), and four in the r band

(u.MP9602 filter). The total exposure time was 2800 s for u and r , and 1200s for g . The dimm mode seeing varied from $0''.51$ to $0''.72$. Data were preprocessed for overscan modeling, bias

subtraction, bad-pixel masking, and flat-fielding, with the ELIXIR software (S. D. J. Gwyn 2008). We then used the IRAF task `imcombine` to create three combined images in the three bands, with cosmic rays filtered out.

3.5. Hubble Space Telescope

The field of NGC 6099 was also observed by the Wide Field Camera 3 (WFC3) on board the Hubble Space Telescope (HST), on 2023 September 5 (PI: I. Chilingarian). Images were taken in three UVIS bands: F300X (exposure time of 696 s), F475W (696 s), and F814W (648 s). We downloaded the drizzled Single Visit Mosaics provided as Hubble Advanced Products, from the Barbara A. Mikulski Archive for Space Telescopes. Detailed analysis and results of those observations will be reported elsewhere (K. Grishin et al. 2025, in preparation). In this paper, we use preliminary results taken from that forthcoming work to constrain the physical size (Section 4) and brightness (Section 5) of the optical counterpart and to improve our X-ray/optical spectral modeling (Section 7).

4. Optical/X-Ray Alignment

To search for an optical counterpart of HLX-1, we improved the astrometric solution of the Chandra and CFHT images, by aligning them onto the same reference frame defined by the Gaia DR3 catalog (Gaia Collaboration 2022). To do so, we searched for Chandra/Gaia point-like associations: we found eight such sources. We determined the centroid positions of those eight Chandra sources in the 0.3–8.0 keV band with the CIAO task `wavdetect`. We then applied the `wcs_match` and `wcs_update` tasks to the Chandra data, to align them onto the Gaia reference frame. This corresponds to a shift in $\Delta R.A. \approx 0''.14$ and $\Delta \text{decl.} \approx 0''.44$ with respect to the uncorrected Chandra astrometry from the data archive. After the correction, the residual 1σ random scatter between optical and X-ray positions is $\approx 0''.18$ in R.A. and $\approx 0''.41$ in decl. The relatively large residual scatter is partly due to the location of the calibration sources: all eight of them are located farther than $4'$ from the ACIS-I aimpoint, in regions where the Chandra PSF is already substantially degraded. However, a substantial contribution to the scatter in decl. comes from only one of the eight reference Gaia sources. From a closer analysis of that source (including our inspection of optical images from the Dark Energy Spectroscopic Instrument Legacy Imaging Surveys; K. J. Duncan 2022), we infer that the source is partly resolved, with two optical peaks separated by $\approx 0''.9$ in decl. The Chandra position appears to correspond to the fainter of the two optical peaks. Given the doubts about the accuracy of the X-ray/optical association in this particular case, we decided to remove this calibration source and use only the other seven. This way, the astrometric shift of the Chandra coordinates with respect to the uncorrected archival data is $\Delta R.A. \approx 0''.12$ and $\Delta \text{decl.} \approx 0''.32$, and the residual scatter is $\approx 0''.19$ in R.A. and $\approx 0''.28$ in decl.

We then used `wavdetect` again to determine the instrumental centroid position of HLX-1 in the astrometrically corrected images and its 1σ uncertainty (due to the limited number of ACIS counts); the latter is $\sigma_{R.A.} \approx 0''.06$, $\sigma_{\text{decl.}} \approx 0''.05$. Combining this measurement uncertainty with the uncertainty in the astrometric alignment, we derive a 1σ error in the absolute location of HLX-1 of $\sigma_{R.A.} \approx 0''.19$,

$\sigma_{\text{decl.}} \approx 0''.28$. In conclusion, the best-fitting position of HLX-1 is R.A. (J2000) = $16^{\text{h}} 15^{\text{m}} 34^{\text{s}} 305(\pm 0''.013)$, decl. (J2000) = $+19^{\circ} 27' 08''.06(\pm 0''.28)$.

Next, we improved the astrometric solution of the CFHT images. We selected 10 point-like reference sources with Gaia positions. We used the IRAF task `ccfind` to match the reference stars in Gaia coordinates to the CFHT images. We then fitted the astrometric solutions (independently for each of the three bands) with the IRAF task `ccmap` in interactive mode, removing the reference stars with the highest residuals. The best-fit plate solution can then be used to update the image coordinate system via the task `ccsetwcs` and convert coordinate lists via the task `cctran`. The typical shifts of the improved astrometric solutions with respect to the raw images are $\Delta R.A. \approx 0''.07$ and $\Delta \text{decl.} \approx 0''.08$ for the *u*-band image, $\Delta R.A. \approx -0''.12$ and $\Delta \text{decl.} \approx -0''.09$ for the image of the *g* band, and $\Delta R.A. \approx 0''.08$ and $\Delta \text{decl.} \approx 0''.23$ for the *r*-band image. For the *u*-band image, we obtained a best-fit solution with a residual 1σ scattering $\sigma_{R.A.} \approx 0''.12$, $\sigma_{\text{decl.}} \approx 0''.10$. For the *g*-band and *r*-band images, the astrometric residuals are $\sigma_{R.A.} \approx 0''.12$, $\sigma_{\text{decl.}} \approx 0''.10$, consistent with those of the *u*-band image.

Associating the astrometrically corrected Chandra position of HLX-1 onto the astrometrically corrected CFHT images, we unambiguously identify a bluish optical counterpart (Figure 1, bottom right panel). The brightness and colors of this source will be discussed in Section 5. The centroid of the optical source (averaged over the three bands) is R.A. (J2000) = $16^{\text{h}} 15^{\text{m}} 34^{\text{s}} 305(\pm 0''.006)$, decl. (J2000) = $+19^{\circ} 27' 08''.16(\pm 0''.10)$, where the errors are 1σ . This optical position is consistent with the independently determined X-ray position.

We can further tighten the association of the Chandra source and its CFHT counterpart with a relative rather than absolute astrometric alignment. We identified 11 point-like X-ray sources in the Chandra image within $5'$ of the ACIS-I aimpoint that have an obvious optical counterpart in the CFHT images; only one of these 11 sources is in the Gaia sample used earlier for absolute astrometric calibration. We used these new reference sources to realign the CFHT image directly onto the Chandra frame. After realignment, the 1σ random scatter between X-ray and optical positions is $\approx 0''.17$ in R.A. and in decl. Thus, the 90% (1.645 σ) error radius of the Chandra position overplotted onto the CFHT images is $\approx 0''.4$ (Figure 4).

Finally, we report preliminary results of the HST/WFC3 observations (K. Grishin et al. 2025, in preparation). The optical counterpart of HLX-1 is detected in all three bands (F300X, F475W, and F814W), at a position consistent with the Chandra position (Figure 5). From the SEXTRACTOR (E. Bertin & S. Arnouts 1996) catalog associated with the F814W data set, the centroid of the optical source is R.A. (J2000) = $16^{\text{h}} 15^{\text{m}} 34^{\text{s}} 300$, decl. (J2000) = $+19^{\circ} 27' 07''.94$, with a centroiding 1σ error radius of $0''.026$ (not including the absolute astrometric uncertainty).

The optical field around HLX-1 is not particularly crowded. There is no other optical source brighter than $m_{g,\text{Vega}} \approx 25$ mag within $4''$ of the assumed optical counterpart. There are four point-like sources brighter than 25 mag within a radius of $\approx 7''$ (area of $\approx 150 \text{ arcsec}^2$). The probability that a point-like X-ray source randomly placed in that field ends up at $\lesssim 0''.3$ of an optical source is $\approx 1/500$. The three strongest IMBH candidates in the catalog of H. Tranin et al. (2022; Section 2.2) are all located in sparsely populated fields near

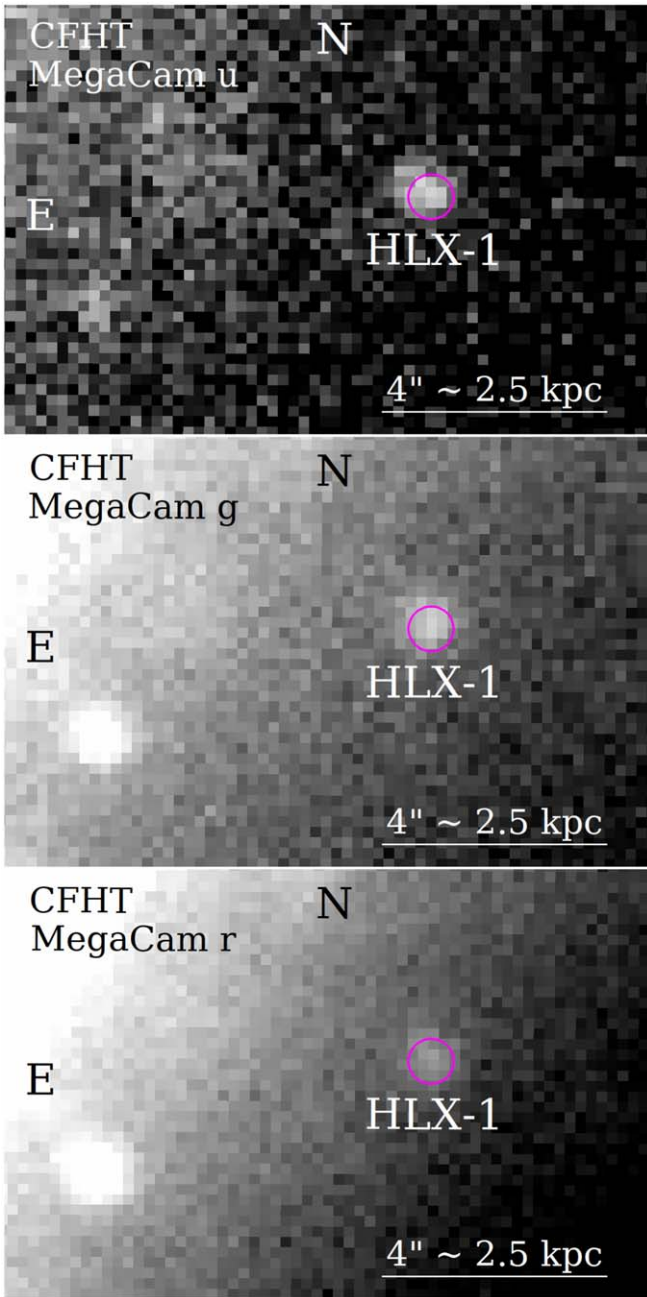


Figure 4. Top: CFHT/MegaCam u -band image (u.MP9302 filter) of the field around HLX-1, taken on 2022 August 2; the 90% error circle (radius of $0''.4$) for the position of the corresponding Chandra source is overplotted in magenta, in all three panels. Middle panel: MegaCam g -band image (g.MP9402 filter). Bottom panel: MegaCam r -band image (r.MP9602 filter).

the outskirts of spheroidal galaxies, and each has a point-like optical counterpart within $\lesssim 0''.3$ of its X-ray position.

5. Optical Brightness

We inspected the radial profile of the optical counterpart of HLX-1 (Section 4) in the CFHT images with DS9. In all three bands, the source is consistent with a 2D Gaussian with a full-width-half-maximum (FWHM) similar to the seeing, i.e., between $\approx 0''.9$ and $\approx 1''.3$. Thus, there is no evidence that the source is extended. From the u band, which has the lowest contamination from the old stellar halo emission of NGC 6099,

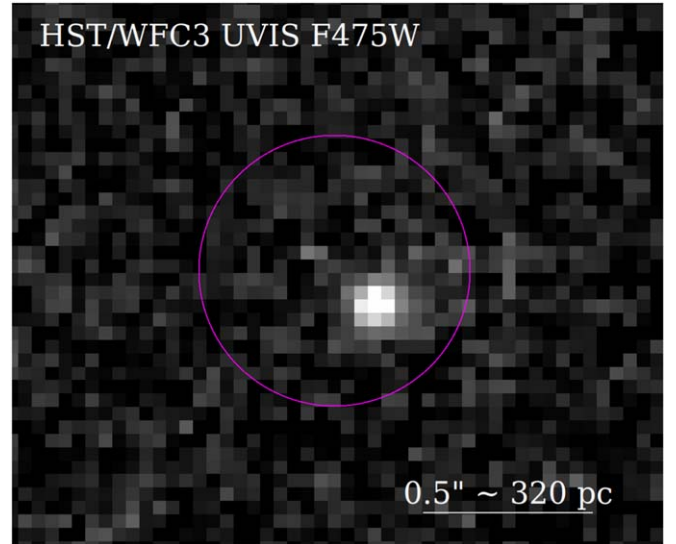


Figure 5. HST/WFC3 UVIS image in the F475W filter. The green circle is the 90% uncertainty on the Chandra source position (radius of $0''.4$). North is up and east is to the left.

we estimate an upper limit of $\approx 0''.9$ in diameter for the optical counterpart. In fact, our preliminary HST investigation shows (K. Grishin et al. 2025, in preparation) that the counterpart appears point-like even in the WFC3 images, implying an angular size $< 0''.15$ in diameter (≈ 100 pc if it is located at the same distance as NGC 6099).

To measure the optical brightness of HLX-1 in the CFHT images, we selected seven nearby point-like sources with known apparent magnitudes, listed in the Sloan Digital Sky Survey (SDSS) DR12 (S. Alam et al. 2015). We converted the AB brightness values from the SDSS u, g, r photometric system to the CFHT Megacam u, g, r system, using the relations in S. D. J. Gwyn (2008).¹⁵ For the seven reference stars, we adopted source extraction radii of $1''.4$ for the u band, $2''.2$ for the g band, and $2''.6$ for the r band; background annuli were taken between $1''.9$ and $2''.6$ in the u band and between $2''.6$ and $3''.6$ for both the g and r bands. For HLX-1, we used a source extraction radius of $1''.3$ in all three CFHT images and a background annulus between $1''.3$ and $2''.2$, to reduce the contamination from the diffuse emission in the halo of NGC 6099. We used the ASTROIMAGEJ multi-aperture differential photometry tool (K. A. Collins et al. 2017) to determine the background-subtracted fluxes from the reference stars and from HLX-1, the latter suitably corrected for its smaller extraction aperture.

For HLX-1, we obtain apparent AB brightnesses $m_{u,AB} = (24.84 \pm 0.12)$ mag, $m_{g,AB} = (24.58 \pm 0.16)$ mag, and $m_{r,AB} = (24.95 \pm 0.32)$ mag (Table 2). The line-of-sight Galactic reddening (J. A. Cardelli et al. 1989; D. J. Schlegel et al. 1998) is $E(B - V) \approx 0.05$ mag. This corresponds to an extinction $A_u \approx 0.22$ mag, $A_g \approx 0.17$ mag, and $A_r \approx 0.11$ mag in the Megacam system (E. F. Schlafly & D. P. Finkbeiner 2011). The low value of the extinction is due to the high Galactic latitude of HLX-1 ($l = 34^\circ 96302$, $b = 42^\circ 81152$). Subtracting the distance modulus of NGC 6099 ($dm \approx 35.72$ mag), we obtain the dereddened absolute brightness

¹⁵ See also <https://www.cadc-ccda.hia-ihp.nrc-cnrc.gc.ca/en/megapipe/docs/filt.html>.

Table 2
Brightness of the Optical Counterpart of HLX-1, Measured from the CFHT Data

Band	t_{exp} (s)	A_{λ} (mag)	m_{AB} (mag)	$m_{\text{AB},0}$ (mag)	$m_{\text{Vega},0}$ (mag)	M_{AB} (mag)	M_{Vega} (mag)	f_{λ} (CGS)	$f_{\lambda,0}$ (CGS)
<i>u</i>	2800.8	0.22	24.84 ± 0.12	24.62 ± 0.12	24.00 ± 0.12	−11.10 ± 0.12	−11.72 ± 0.12	9.33 ± 1.03	11.4 ± 1.3
<i>g</i>	1200.4	0.17	24.58 ± 0.16	24.41 ± 0.16	24.50 ± 0.16	−11.31 ± 0.16	−11.22 ± 0.16	7.03 ± 1.02	8.22 ± 1.19
<i>r</i>	2800.8	0.11	24.95 ± 0.32	24.84 ± 0.32	24.66 ± 0.32	−10.88 ± 0.32	−11.06 ± 0.32	2.80 ± 0.83	3.10 ± 0.91

Note. We report both the observed values (m_{AB}) and those corrected for a line-of-sight Galactic reddening $E(B - V) = 0.05$ mag ($m_{\text{AB},0}$, $m_{\text{Vega},0}$). The conversion from AB to Vega magnitudes is based on the coefficients listed on the MegaPrime/MegaCam website. The absolute magnitudes M_{AB} and M_{Vega} are dereddened values. The flux densities f_{λ} (observed) and $f_{\lambda,0}$ (dereddened) are in units of 10^{-19} erg cm $^{-2}$ sec $^{-1}$ Å $^{-1}$.

$M_{u,\text{AB}} = (-11.10 \pm 0.12)$ mag, $M_{g,\text{AB}} = (-11.31 \pm 0.16)$ mag, and $M_{r,\text{AB}} = (-10.88 \pm 0.32)$ mag. We also provide (Table 2) the apparent and absolute brightness in the Vega system. The conversion from AB to Vega magnitudes is based on the coefficients listed on the MegaPrime/MegaCam website.¹⁶ Moreover, we provide an approximate conversion to the Johnson–Cousins UBV system, using the color transformations of S. D. J. Gwyn (2008) between the MegaCam and SDSS systems, and then the relations of K. Jordi et al. (2006) between the SDSS and Johnson–Cousins systems. We estimate $U_0 = (23.7 \pm 0.2)$ mag, $B_0 = (24.5 \pm 0.2)$ mag, and $V_0 = (24.6 \pm 0.2)$ mag (corrected for line-of-sight reddening).

Finally, we measured the source brightness from the HST/WFC3 observations (K. Grishin et al. 2025, in preparation), in three bands (F300X, F475W, and F814W). The HST images were taken 13 months after the CFHT images; thus, in principle, the source may have varied between the two data sets. The apparent brightnesses (AB mag system)¹⁷ are $m_{\text{F300X,AB}} = (25.14 \pm 0.05)$ mag in the F300X band (broad UV), $m_{\text{F475W,AB}} = (24.62 \pm 0.05)$ mag in the F475W band (similar to the SDSS g' band and, roughly, to the B band), and $m_{\text{F814W,AB}} = (24.57 \pm 0.05)$ mag in the F814W band (similar to the I band). All those values were already corrected for line-of-sight Galactic extinction. Converting to the Vegamag system, and applying a distance modulus of 35.72 mag, those values correspond to extinction-corrected absolute magnitudes $M_{\text{F300X,Vega}} = (-11.99 \pm 0.05)$ mag, $M_{\text{F475W,Vega}} \approx M_{g',\text{Vega}} = (-11.00 \pm 0.05)$ mag, and $M_{\text{F814W,Vega}} \approx M_I = (-11.58 \pm 0.05)$ mag. In terms of the standard (dereddened) colors in the Johnson–Cousins system, putting together CFHT and HST results, we estimate $U - B = (-0.8 \pm 0.3)$ mag, $B - V = (-0.1 \pm 0.3)$ mag, and $V - I = (0.5 \pm 0.2)$ mag.

6. X-Ray Results

6.1. Chandra Spectrum from 2009

The 2009 Chandra spectrum of HLX-1 has only ≈ 50 net counts. This is enough for simple one-component spectral modeling, such as a power law or disk blackbody (Table 3). In all cases, we fit the spectra with the Cash statistics.

First, we tried a power-law model absorbed only by the line-of-sight Galactic column density. We used the Tuebingen–Boulder photoelectric absorption model (TBABS in XSPEC) for this and all other X-ray spectral modeling in this work. We applied the “wilm” abundance table (J. Wilms et al. 2000)

from XSPEC. We adopted the Galactic line-of-sight neutral hydrogen column density $N_{\text{H}} = 4.16 \times 10^{20}$ cm $^{-2}$, obtained from the COLDEN¹⁸ online tool, based on the radio maps of J. M. Dickey & F. J. Lockman (1990). Alternative online tools for the estimation of the hydrogen column density give values ranging from $N_{\text{H}} = 3.7 \times 10^{20}$ cm $^{-2}$ (HEASARC’s NH tool,¹⁹ based on the HI4PI Collaboration et al. 2016 map) to $N_{\text{H}} = 4.4 \times 10^{20}$ cm $^{-2}$ (Swift Science Data Center’s NHTOT tool,²⁰ based on the maps of P. M. W. Kalberla et al. 2005, but including also a contribution from molecular hydrogen, as described in R. Willingale et al. 2013). The difference between those alternative choices is negligible for our analysis. The photon index of our best-fitting power-law model (ABS PL in Table 3) is $\Gamma = 3.8 \pm 0.6$. The absorbed 0.3–10 keV flux is $f_{\text{X}} = (2.2^{+0.6}_{-0.4}) \times 10^{-14}$ erg cm $^{-2}$ s $^{-1}$ and the corresponding unabsorbed luminosity is $L_{\text{X}} = (8.1^{+2.1}_{-2.3}) \times 10^{40}$ erg s $^{-1}$. The fit statistics is Cstat = 32 over 47 degrees of freedom (dof). To assess whether the inclusion of an additional free intrinsic absorption component significantly improves the model, we created a set of 1000 simulated data sets with the `simfittest` script in XSPEC; we verified that such an additional component is not required.

The steep value of the photon index for the power-law model suggests that a thermal model is physically more plausible; the latter should also provide a better estimate of the intrinsic luminosity, because it does not diverge at the lower-energy end. Therefore, we tried fitting the same spectrum with the standard multicolor blackbody model (`diskbb` in XSPEC). Such a model with only line-of-sight absorption returns a peak color temperature $kT_{\text{in}} = (0.22^{+0.05}_{-0.04})$ keV and a normalization corresponding to an apparent inner-disk radius of $r_{\text{in}} = (11, 300^{+1,600}_{-1,400}) (\cos \theta)^{-1/2}$ km at the distance of NGC 6099 (ABS DBB in Table 3). A “true” inner-disk radius of $R_{\text{in}} \approx 1.19 r_{\text{in}}$ (A. Kubota et al. 1998) is often used in the X-ray modeling of accretion disks, where the correction factor takes into account the no-torque inner-boundary condition and the ratio between the color temperature and the effective temperature (hardening factor); the value of 1.19 corresponds to a “standard” hardening factor $f \approx 1.7$ (T. Shimura & F. Takahara 1995; A. Merloni et al. 2000; S. W. Davis & S. El-Abd 2019). With this approximation, the true inner-disk radius is $R_{\text{in}} = (13, 400^{+1,900}_{-1,600}) (\cos \theta)^{-1/2}$ km. The absorbed 0.3–10 keV flux is $f_{\text{X}} = (1.5^{+0.2}_{-1.2}) \times 10^{-14}$ erg cm $^{-2}$ s $^{-1}$ and the unabsorbed luminosity is $L_{\text{X}} = (4.4^{+1.3}_{-1.1}) \times 10^{40}$ erg s $^{-1}$. The fit statistic is Cstat = 31/47 dof. In this case, too, the addition of a free intrinsic absorption component does not lead to a statistical

¹⁶ <https://www.cfht.hawaii.edu/Instruments/Imaging/Megacam/specinformation.html>.

¹⁷ <https://www.stsci.edu/hst/instrumentation/wfc3/data-analysis/photometric-calibration/uvis-photometric-calibration>

¹⁸ <https://cxc.harvard.edu/toolkit/colden.jsp>.

¹⁹ <https://heasarc.gsfc.nasa.gov/cgi-bin/Tools/w3nh/w3nh.pl>.

²⁰ <https://www.swift.ac.uk/analysis/nhtot/docs.php>.

Table 3
X-Ray Spectral Parameters of HLX-1 for Selected Models

Observation (1)	Model (2)	Spectral Parameters (3)	Statistic/dof (4)	F_x (5)	L_x (6)
Chandra	ABS PL	$N_{\text{H,int}} = [0]$ $\Gamma = 3.8 \pm 0.6$ $N_{\text{pl}} = 0.43^{+0.11}_{-0.10}$	32/47	$0.22^{+0.06}_{-0.04}$	$0.81^{+0.21}_{-0.23}$
	ABS DBB	$N_{\text{H,int}} = [0]$ $kT_{\text{in}} = 0.22^{+0.05}_{-0.04}$ $N_{\text{disk}} = 0.66^{+0.16}_{-0.13}$	31/47	$0.15^{+0.02}_{-0.12}$	$0.44^{+0.13}_{-0.11}$
	ABS DAPEC	$N_{\text{H,int}} = [0]$ $kT_1 = 0.16^{+0.07}_{-0.11}$ $N_{\text{ap1}} = 2.3^{+1.9}_{-1.5}$ $kT_2 = 1.24^{+0.49}_{-0.27}$ $N_{\text{ap2}} = 0.50^{+0.24}_{-0.16}$	30/45	$0.19^{+0.07}_{-0.12}$	$0.62^{+0.16}_{-0.17}$
XMM1	ABS (PL+DBB)	$N_{\text{H,int}} = 0.07 \pm 0.03$ $\Gamma = 3.9 \pm 0.3$ $N_{\text{pl}} = 15.0^{+3.8}_{-3.6}$ $kT_{\text{in}} = 0.25^{+0.03}_{-0.02}$ $N_{\text{disk}} = 7.96^{+6.56}_{-3.96}$	275/256	$7.41^{+0.17}_{-0.26}$	39.3 ± 5.7
	ABS (SIMPL+DBB)	$N_{\text{H,int}} = 0.01^{+0.02}_{-0.01}$ $\Gamma = 4.6^{+0.2}_{-0.4}$ FrSc > 0.59 UpSc = [0] $kT_{\text{in}} = 0.16 \pm 0.02$ $N_{\text{disk}} = 91^{+68}_{-35}$	281/256	$7.56^{+0.11}_{-2.80}$	$23.1^{+3.3}_{-3.4}$
XMM2	ABS PL	$N_{\text{H,int}} = 0.09^{+0.07}_{-0.05}$ $\Gamma = 3.7^{+0.6}_{-0.5}$ $N_{\text{pl}} = 0.51^{+0.11}_{-0.08}$	41/49	0.15 ± 0.02	0.85 ± 0.15
	ABS DBB	$N_{\text{H,int}} < 0.02$ $kT_{\text{in}} = 0.24 \pm 0.03$ $N_{\text{disk}} = 0.33^{+0.20}_{-0.12}$	53/49	$0.12^{+0.02}_{-0.01}$	$0.37^{+0.06}_{-0.07}$
	ABS (PL+DBB)	$N_{\text{H,int}} = 0.19^{+0.08}_{-0.12}$ $\Gamma = 3.6^{+0.4}_{-0.8}$ $N_{\text{pl}} = 0.55^{+0.07}_{-0.20}$ $kT_{\text{in}} = 0.07 \pm 0.01$ $N_{\text{disk}} = 850^{+856}_{-725}$	37/47	$0.14^{+0.04}_{-0.03}$	1.1 ± 0.3

Note. Errors are 90% confidence limits for one interesting parameter. All models include a line-of-sight absorption $N_{\text{H}} = 4.16 \times 10^{20} \text{ cm}^{-2}$, in addition to the intrinsic absorption listed here. Column (1): see Table 1 for the observation log. Column (2): the shorthand notation for model components is ABS = T_{babs}, PL = power law, DBB = disk blackbody, DAPEC = two-temperature apec, and SIMPL = Comptonization model. In addition, the XMM-Newton spectra include a contamination component from the diffuse gas emission of NGC 6099, modeled as a fraction C of the total emission modeled from the Chandra data, namely $C \times \text{Tbabs} \times \text{Tbabs}_{\text{int}} \times \text{apec}$. For XMM1, $C \equiv 0.06$; for XMM2, $C \equiv 0.04$. Column (3): $N_{\text{H,int}}$ is in units of 10^{22} cm^{-2} ; N_{pl} is in units of 10^{-5} photons $\text{keV}^{-1} \text{ cm}^{-2} \text{ s}^{-1}$ at 1 keV; kT_{in} , kT_1 , and kT_2 are in units of kiloelectronvolts; $N_{\text{disk}} \equiv (r_{\text{in}}/D_{10})^2 \cos \theta$, where r_{in} is the apparent inner-disk radius in kilometers and D_{10} is the distance in units of 10 kpc; N_{ap1} and N_{ap2} are 10^{-5} times the XSPEC apec model normalization explained at <https://heasarc.gsfc.nasa.gov/xanadu/xspec/manual/node134.html>. Column (4): the fit statistics are Cstat for Chandra and χ^2 for XMM1 and XMM2. Column (5): 0.3–10 keV model of absorbed flux, in units of $10^{-13} \text{ erg cm}^{-2} \text{ s}^{-1}$, with a 90% confidence interval. Column (6): 0.3–10 keV unabsorbed isotropic luminosity, in units of $10^{41} \text{ erg s}^{-1}$, with a 90% confidence interval.

improvement of the fit. The disk blackbody fit is statistically equivalent to the power-law fit, although we consider the thermal model more physical for an accreting compact object in a soft state. More generally, accreting compact objects are typically modeled with thermal plus nonthermal components (e.g., a disk blackbody plus power law) or Comptonization models. In the case of our 2009 Chandra observations, the number of counts is too low and the systematic uncertainties are too high to effectively constrain such multicomponent models. We verified with a

simftest analysis that the addition of a second component does not improve the single-component fits.

Another possibility, sometimes usefully applied to ULX spectra (D. J. Walton et al. 2018b, 2020; F. Barra et al. 2024), is a double thermal model (e.g., blackbody plus blackbody). One component may correspond to the outer (standard) disk emission, the other to the innermost (advective) part of the disk; alternatively, they may be interpreted as emission from the disk and from the photosphere of an optically thick outflow.

Guided by this possible physical interpretation, we tried fitting a double-blackbody model with fixed line-of-sight absorption. The fit statistics ($Cstat = 30/45$ dof) is equivalent to those of the power-law and disk blackbody models; in this case, too, the addition of a free intrinsic absorption component ($Cstat = 29/44$ dof) does not improve the fit. One thermal component is well constrained, with $kT_1 = (0.18^{+0.02}_{-0.03})$ keV, radius $R_{bb,1} = (16, 400 \pm 6, 800)$ km, and unabsorbed isotropic 0.3–10 keV luminosity $L_{bb,1} = (3.6^{1.3}_{1.0}) \times 10^{40}$ erg s $^{-1}$. The second (cooler) thermal component is unconstrained and its presence does not improve the fit.

Finally, we considered the possibility that the emission is due to an optically thin thermal plasma (for example, in the case of shocked gas), and we fitted the 2009 Chandra spectrum with a double-temperature `apec` model (ABS DAPEC in Table 3 and Figure 6), with fixed redshift $z = 0.03$ and fixed solar abundances. We obtain good fits ($Cstat = 30/45$ dof), for example, with fixed line-of-sight absorption and plasma temperature components $kT_1 = (0.16^{+0.07}_{-0.11})$ keV and $kT_2 = (1.24^{+0.49}_{-0.27})$ keV, corresponding to an unabsorbed 0.3–10 keV luminosity $L_X = (6.2^{+1.6}_{-1.7}) \times 10^{40}$ erg s $^{-1}$. In summary, all the models listed in Table 3 are equally acceptable fits of the 2009 Chandra spectrum, although they are associated with different physical interpretations.

In addition to the study of HLX-1, we used the Chandra data to extract and model the spectrum of the diffuse emission around the nucleus and innermost region of NGC 6099. The spectrum is well described ($Cstat = 50$ for 66 dof) by a single-temperature, solar-abundance `apec` model, with fixed redshift ($z = 0.03$), fixed line-of-sight Galactic absorption, and best-fitting $N_{H,int} = (5.7^{+0.4}_{-0.3}) \times 10^{21}$ cm $^{-2}$. The best-fitting plasma temperature is $kT = (0.37^{+0.27}_{-0.16})$ keV, with an observed 0.3–10 keV flux of $f_X = (1.6^{+0.2}_{-0.4}) \times 10^{-14}$ erg cm $^{-2}$ s $^{-1}$. In the Chandra images (Figure 1, bottom left panel), HLX-1 is sufficiently far away and the ACIS PSF is sufficiently sharp to avoid any contamination from the diffuse galaxy emission. However, this is not necessarily the case for the subsequent XMM-Newton observations. By modeling the extent, spectral shape, and flux of the diffuse gas emission from the Chandra data, we will constrain its contamination to the HLX-1 emission in the XMM-Newton data.

6.2. XMM-Newton Spectra from 2012

In the 2012 XMM-Newton observations, the flux from HLX-1 dramatically increased by a factor of about 50 compared with 2009, to the point that it was now completely dominant over the diffuse galactic emission. Generally speaking, we need to carefully assess cross-contamination in a situation where the distance between HLX-1 and the nucleus of NGC 6099 is comparable to the half-energy width of the on-axis PSF of MOS1, MOS2, and pn (S. L. O’Dell et al. 2010). To quantify the amount of residual contamination, we estimated what fraction of the diffuse galactic emission falls within the 14 $''$ 5 source extraction circle of HLX-1. For this, we took the spatial extent of the diffuse emission from the Chandra observations and convolved it with the EPIC-MOS and EPIC-pn PSFs. We estimate that $\approx 6\%$ of the diffuse gas emission falls inside the HLX-1 source region. Therefore, we include this component by rescaling the normalization of the best-fitting thermal plasma model for the 2009 Chandra data (Section 6.1). In any case, the galactic contamination contributes an insignificant flux of

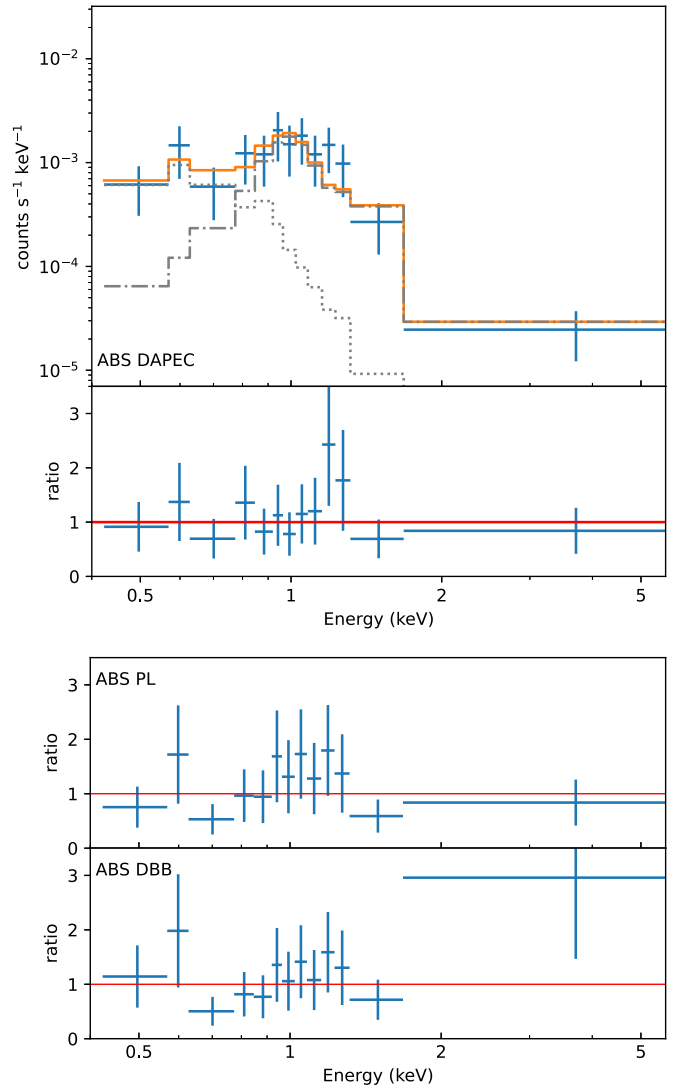


Figure 6. Top two panels: 2009 Chandra/ACIS background-subtracted, folded spectrum, fitted with a double `apec` model, and corresponding data/model ratios. The data have been fitted with the Cash (Wstat) statistics. They have been subsequently grouped to a minimum signal-to-noise ratio of 1.8 for plotting purposes only. See Table 3 for the best-fitting parameters. Bottom two panels: data/model ratios for the same Chandra/ACIS spectrum, fitted with alternative models (Table 3): from top to bottom, a power-law and a disk blackbody model.

$\approx 10^{-15}$ erg cm $^{-2}$ s $^{-1}$ to the 2012 spectra, compared with the observed source flux of $\approx 7 \times 10^{-13}$ erg cm $^{-2}$ s $^{-1}$.

The 2012 data set is the only one where we have a high enough signal-to-noise ratio to attempt also a timing analysis. We searched for periodicities or quasiperiodic oscillations with standard tasks in the FTOOLS package (`efsearch` and `powspec`, respectively), in the 1–10,000 s range, but did not find any. Following standard usage (e.g., S. Vaughan et al. 2003; L. M. Heil et al. 2012; A. D. Sutton et al. 2013; M. J. Middleton et al. 2015; A. Robba et al. 2021), we measured the normalized excess variance in the pn light curve (binned to 100 s) to quantify the short-term flux variability, with the FTOOLS task `lcstats`. In particular, the fractional root mean square (rms) variability amplitude is the square root of the normalized excess variance. We estimate an rms of $(20 \pm 2)\%$. We leave further investigations on the X-ray timing

properties to follow-up work; here, we focus instead on the spectral properties.

For our spectral analysis, we fitted the pn, MOS1, and MOS2 data simultaneously, with the χ^2 statistics. We tested two simple phenomenological models: a power law and a disk blackbody, both with fixed line-of-sight absorption plus free intrinsic absorption. For the absorbed power-law fit, we obtained $\chi^2 = 312$ (258 dof), while for the absorbed disk blackbody fit, we obtained $\chi^2 = 375$ (258 dof). Both models fail to describe the data and are rejected at the 2.5σ and 4.7σ levels, respectively.

Significantly better results are obtained with an absorbed PL-plus-DBB model (see Table 3 for the fit parameters and the upper panel of Figure 7 for a plot of the model fit and residuals): with a statistic of $\chi^2 = 275$ (256 dof), the model is acceptable within the 90% confidence level. The thermal disk component has a peak color temperature $kT_{\text{in}} = 0.25^{+0.03}_{-0.02}$ keV and an apparent inner-disk radius $r_{\text{in}} = (39, 200^{+16,400}_{-10,200}) (\cos \theta)^{-1/2}$ km (i.e., $R_{\text{in}} = (46, 700^{+19,500}_{-12,100}) (\cos \theta)^{-1/2}$ km). The power-law component has a steep photon index $\Gamma = 3.9 \pm 0.3$. The unabsorbed luminosity in the 0.3–10 keV band is $L_X \approx (3.9 \pm 0.6) \times 10^{42}$ erg s $^{-1}$.

We then explored another fitting model often used for soft-state ULXs. We replaced the standard disk with a p -free disk (`diskpbb` in XSPEC), in which the temperature scales as $T \propto R^{-p}$ instead of $T \propto R^{-0.75}$ (S. Mineshige et al. 1994; K.-y. Watarai et al. 2000; A. Kubota & K. Makishima 2004; A. Kubota et al. 2005). This “broadened disk” is a well-known approximation of an advection-dominated, supercritical slim disk, with a reduced radiative efficiency in the inner region. Typical values of $p \approx 0.6$ are found in supercritical disks (K. Vierdayanti et al. 2008; A. D. Sutton et al. 2017). In our case, we find a best-fitting value $p \approx 0.6$, but the whole range $0.5 \lesssim p \lesssim 1.0$ is acceptable within the 90% confidence limit. Thus, the model is indistinguishable from a standard disk blackbody with $p = 0.75$. The goodness-of-fit parameter $\chi^2 = 275$ (255 dof) is unchanged. The main reason why we cannot distinguish between power law plus standard disk and power law plus p -free disk is that most of the emission is in the power-law component.

Finally, we tried Comptonization models, as a more physical representation of the thermal-plus-nonthermal spectrum. We found better fits with models based on multitemperature thermal seed components, such as `diskir` (M. Gierliński et al. 2008, 2009) and `simpl` (J. F. Steiner et al. 2009), rather than single-temperature blackbody seeds, such as `comptt` and `bmc`. For the `simpl*diskbb` model, we confirm a very steep power-law slope ($\Gamma = 4.6^{+0.2}_{-0.4}$), with a slightly lower peak temperature ($kT_{\text{in}} = 0.16 \pm 0.02$ keV) compared with that found in the power-law-plus-disk-blackbody model. The apparent inner radius is $r_{\text{in}} = (132, 000^{+43,000}_{-28,000}) (\cos \theta)^{-1/2}$ km (i.e., $R_{\text{in}} = (158, 000^{+51,000}_{-34,000}) (\cos \theta)^{-1/2}$ km; ABS (SIMPL*DBB) in Table 3). The unabsorbed 0.3–10 keV luminosity is $L_X = (2.3 \pm 0.3) \times 10^{42}$ erg s $^{-1}$. Essentially identical parameters are obtained with `diskir`: $\Gamma = 4.3^{+0.4}_{-0.3}$, $kT_{\text{in}} = 0.16^{+0.04}_{-0.03}$ keV, $L_X = (2.3 \pm 0.3) \times 10^{42}$ erg s $^{-1}$. In summary, Comptonization models (`simpl` model: $\chi^2 = 281/256$ dof; `diskir` model: $\chi^2 = 283/253$ dof) do not provide better fits than the disk-blackbody-plus-power-law model, but they are still acceptable at the 90% confidence level. Additionally, unabsorbed luminosities estimated from Comptonization models are more reliable, because they avoid the unphysical divergence of the steep power law at the low-energy end.

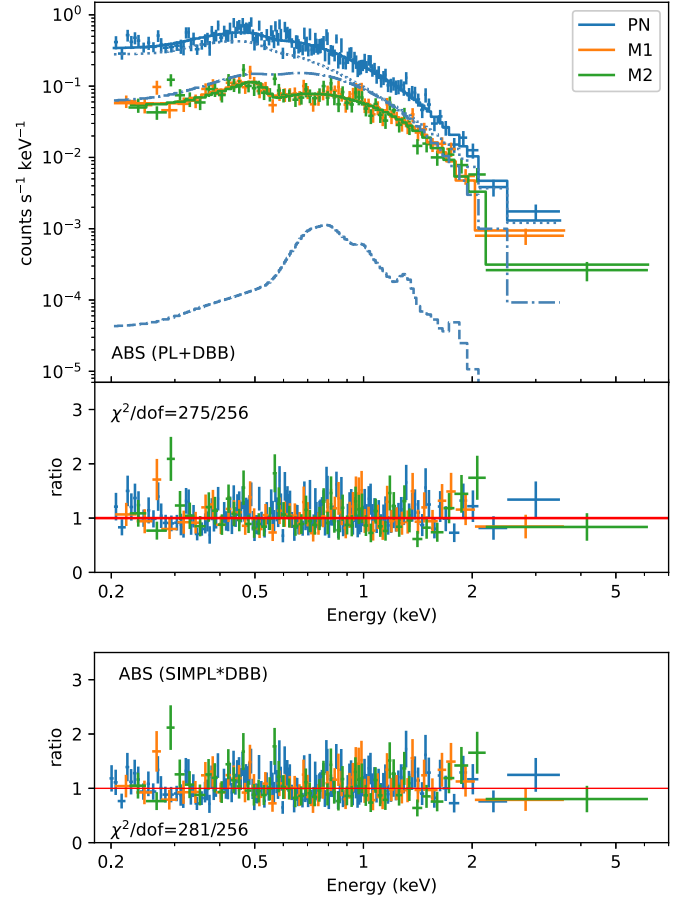


Figure 7. Top two panels: 2012 XMM-Newton/EPIC background-subtracted, folded spectra (blue: pn; orange: MOS1; and green: MOS2), simultaneously fitted with a disk-blackbody-plus-power-law model, and corresponding data/model ratios. The dotted line shows the power-law contribution for the pn, and the dashed-dotted line is the disk blackbody contribution. The dashed line represents our estimated (fixed) contamination from the diffuse gas in NGC 6099; its inclusion and assumed shape do not significantly affect any of the the best-fitting parameters. The data have been binned to a minimum of 20 counts per bin, for χ^2 fitting. See Table 3 for the best-fitting parameters (XMM1 observation, ABS (PL+DBB) model). Bottom panel: data/model ratios for the same XMM-Newton/EPIC spectra, fitted with Comptonization model (ABS (SIMPL*DBB) in Table 3).

6.3. XMM-Newton Spectra from 2023

In 2023, the observed X-ray flux of HLX-1 was back at a level similar to that of 2009 (Table 3). To account for contamination from the NGC 6099 diffuse emission, we followed the procedure outlined in Section 6.2. Since the X-ray flux of HLX-1 in 2023 was significantly lower than in 2012, optimizing the signal-to-noise ratio required the use of a smaller source region, with a radius of $10''$. We estimate that this region includes approximately 4% of the total diffuse emission from the galaxy, and we have accordingly rescaled the normalization to account for this leakage. The presence of this galaxy component is implicit in the fit results of Table 3, where we only list the fit parameters for the HLX-1 emission.

We started again from simple one-component models (power law and disk blackbody) and then a combined power-law-plus-disk-blackbody model. We tested the significance of additional free intrinsic absorption with the likelihood ratio test `simftest`. For the disk blackbody model, intrinsic absorption

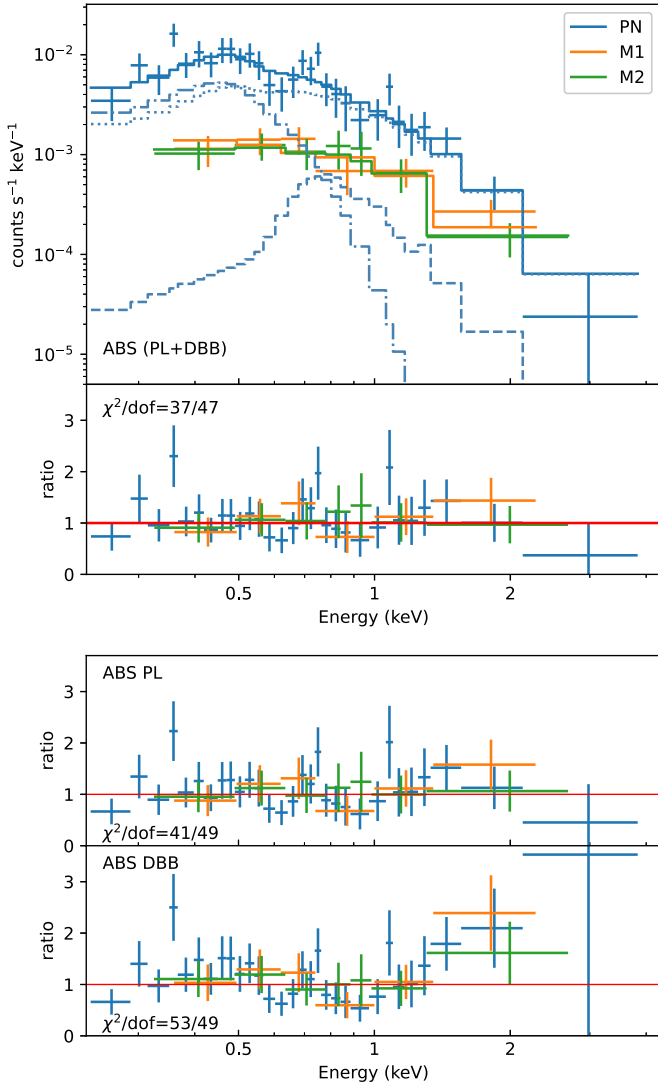


Figure 8. Top two panels: 2023 XMM-Newton/EPIC background-subtracted, folded spectra (blue: pn; orange: MOS1; and green: MOS2), simultaneously fitted with a disk-blackbody-plus-power-law model, and corresponding data/model ratios. The dotted line shows the power-law contribution for the pn, and the dashed-dotted line is the disk blackbody contribution. The dashed line represents our estimated (fixed) contamination from the diffuse gas in NGC 6099. The data have been binned to a minimum of 20 counts per bin, for χ^2 fitting. See Table 3 for the best-fitting parameters (XMM2 observation, ABS (PL+DBB) model). Bottom two panels: data/model ratios for the same XMM-Newton/EPIC spectra, fitted with two alternative models: a power-law model and a disk blackbody model.

is not required. For models that include a power law, intrinsic absorption is required at the 99% confidence level.

All three models (power law, disk blackbody, and power law plus disk blackbody) give acceptable fits (Table 3). The upper panel of Figure 8 shows the combined model (disk blackbody plus power law) fit along with the residuals, while the lower panel displays the residuals for the power-law and disk-blackbody models separately. The power-law model has a steep slope $\Gamma = 3.7^{+0.6}_{-0.5}$ (Table 3), and the addition of intrinsic absorption avoids a divergence from the observed flux at the low-energy end. When a disk blackbody component ($kT_{\text{in}} = (0.07 \pm 0.01)$ keV) is also added, there is an inevitable degeneracy between the strength of the soft thermal component and the amount of intrinsic absorption.

The power-law-plus-disk-blackbody model is generally preferred for physical reasons, but it may overestimate the unabsorbed luminosity. Instead, a pure disk blackbody model with $kT_{\text{in}} = (0.24 \pm 0.03)$ keV provides a better estimate of the intrinsic luminosity, because of its more physical turnover at low energies.

For a pure disk blackbody model, the apparent inner-disk radius is $r_{\text{in}} = (8,000^{+2,100}_{-1,600}) (\cos \theta)^{-1/2}$ km ($R_{\text{in}} = (9,500^{+2,500}_{-1,900}) (\cos \theta)^{-1/2}$ km), marginally consistent with the characteristic emission radius from the 2009 observation. Instead, for the power-law-plus-disk-blackbody model, the thermal component is only a nondominant correction to the power-law emission; in that case, the radius of the thermal component is poorly constrained and degenerate with the intrinsic absorption. The unabsorbed, isotropic 0.3–10 keV luminosity is $L_X = (3.7^{+0.6}_{-0.7}) \times 10^{40}$ erg s⁻¹ for the disk blackbody fit, while it is $L_X \approx 10^{41}$ erg s⁻¹ for models dominated by the steep power law.

Finally, we tried two Comptonization models: *diskirr* and *simpl*. In both cases, we obtain statistically equivalent fits to the simple power-law model ($\chi^2 = 37$ over 45 dof for *diskirr*, $\chi^2 = 37$ over 47 dof for *simpl*, and $\chi^2 = 41$ over 49 dof for a simple power law), because the signal-to-noise ratio and the number of data points are too low to require complex multicomponent fitting. At the high-energy end, because of the steep spectral slope ($\Gamma > 3$), it is not possible to determine whether the spectrum steepens even further (break or exponential cutoff) above a few kiloelectronvolts, as is usually the case for super-Eddington stellar-mass ULXs (D. J. Walton et al. 2018b, 2018a). At the low-energy end, the temperature of the seed thermal component is again degenerate with the amount of intrinsic absorption. For the *diskirr* model, we obtained an intrinsic column density $N_{\text{H,int}} = (1.2^{+0.7}_{-0.6}) \times 10^{21}$ cm⁻², a peak color temperature $kT_{\text{in}} = (0.08^{+0.01}_{-0.03})$ keV, and a photon index $\Gamma = 3.4^{+0.7}_{-0.4}$ (Table 4). The apparent inner-disk radius is $r_{\text{in}} = (164,000^{+167,000}_{-50,000}) (\cos \theta)^{-1/2}$ km ($R_{\text{in}} = (195,000^{+99,000}_{-60,000}) (\cos \theta)^{-1/2}$ km). The unabsorbed luminosity is $L_X = (1.0 \pm 0.2) \times 10^{41}$ erg s⁻¹. For the *simpl* × *diskbb* model, $N_{\text{H,int}} = (1.7^{+0.5}_{-1.0}) \times 10^{21}$ cm⁻², $kT_{\text{in}} = (0.07^{+0.01}_{-0.04})$ keV, and $\Gamma = 3.6^{+0.9}_{-0.3}$ (Table 5). The inner-disk radius is $r_{\text{in}} = (370,000^{+223,000}_{-139,000}) (\cos \theta)^{-1/2}$ km ($R_{\text{in}} = (440,000^{+265,000}_{-165,000}) (\cos \theta)^{-1/2}$ km). The unabsorbed luminosity is $L_X \approx (1.6 \pm 0.3) \times 10^{41}$ erg s⁻¹. An important caveat of both Comptonization models is that the best-fitting radius of the thermal component is much larger than the radius obtained from a disk blackbody model. Physically, such radii may represent the size of the Comptonizing region rather than the innermost stable orbit. We will use Comptonization models again in Section 7, to match the UV/optical data to the soft X-ray data, because such models avoid an unphysical low-energy divergence of the power-law component.

6.4. X-Ray Comparison between 2009 and 2023

The 2009 Chandra and 2023 XMM-Newton spectra have similar fluxes and luminosities (Table 3), within the uncertainties of the various models. It is natural to test whether HLX-1 had “returned” to the same X-ray state of 2009 in 2023, after an outburst in between those years. To test this possibility, we tried fitting simultaneously the 2009 and 2023 spectra, locking all parameters. A short discussion of the disk blackbody model fit will suffice to illustrate the result. We find (Figure 9) a perhaps surprisingly good fit, with $C_{\text{stat}} = 93$ (31 + 62 from

Table 4

Optical/X-Ray SED from the 2022–2023 Data, Fitted with an Irradiated Disk Model: $\text{redden} \times \text{redden}_{\text{int}} \times \text{TBabs} \times (\text{TBabs}_{\text{int}} \times \text{diskir}[+0.04 \times \text{TBabs}_{\text{gal}} \times \text{apec}_{\text{gal}}])$

Component	Parameter	Value	Unit
$\text{redden}_{\text{int}}$	$E(B - V)$	$0.11^{+0.21}_{-0.07}$	mag
$\text{TBabs}_{\text{int}}$	$N_{\text{H,int}}$	$0.12^{+0.07}_{-0.06}$	10^{22} cm^{-2}
diskir	kT_{in}	$0.08^{+0.01}_{-0.03}$	keV
	Γ	$3.4^{+0.7}_{-0.4}$...
	kT_{c}	[100]	keV
	$L_{\text{c}}/L_{\text{d}}$	$0.22^{+1.08}_{-0.12}$...
	f_{in}	[0.1]	...
	r_{irr}	[1.2]	...
	f_{out}	$0.03^{+0.07}_{-0.01}$...
$\text{TBabs}_{\text{gal}}$	$\log(R_{\text{out}})^{\text{a}}$	$3.49^{+0.21}_{-0.42}$	See notes
	$N_{\text{disk}}^{\text{b}}$	140^{+427}_{-73}	km^2
	$N_{\text{H,gal}}$	[0.57]	10^{22} cm^{-2}
apecgal	kT	[0.37]	keV
	$N_{\text{apec}}^{\text{c}}$	[6.85]	See notes
χ^2/dof		41/50	
$R_{\text{in}}\sqrt{\cos\theta}$		$19.5^{+29.9}_{-5.3}$	10^9 cm
F_{X}^{d}		$1.4^{+0.1}_{-0.3} \times 10^{-14}$	$\text{erg cm}^{-2} \text{ s}^{-1}$
L_{X}^{e}		$1.1^{+0.2}_{-0.2} \times 10^{41}$	erg s^{-1}

Notes. The last term accounts for the contamination of thermal emission from the host galaxy NGC 6099; we did not include this term in the flux and luminosity of HLX-1. The errors are 90% confidence limits for one interesting parameter. The X-ray line-of-sight absorption is $N_{\text{H}} \equiv 4.16 \times 10^{20} \text{ cm}^{-2}$; the line-of-sight reddening is $E(B - V) \equiv 0.05 \text{ mag}$.

^a The outer-disk radius R_{out} is in units of the apparent inner-disk radius r_{in} ; the physical inner-disk radius $R_{\text{in}} \approx 1.19r_{\text{in}}$ (A. Kubota et al. 1998).

^b The disk normalization N_{disk} and inner-disk radius R_{in} are related by $R_{\text{in}}\sqrt{\cos\theta} \approx 1.19\sqrt{N_{\text{disk}}}d_{10}$, where $d_{10} = 13,900$ is the distance in units of 10 kpc.

^c N_{apec} is defined here as 10^{-5} times the XSPEC *apec* model normalization.

^d Absorbed flux in the 0.3–10 keV band.

^e Unabsorbed isotropic luminosity in the 0.3–10 keV band.

the 2009 and 2023 data points, respectively) over 98 dof. The intrinsic absorption column density is negligible ($N_{\text{H,int}} < 2 \times 10^{20} \text{ cm}^{-2}$). The best-fitting peak color temperature is $kT_{\text{in}} = (0.24 \pm 0.02) \text{ keV}$. The disk normalization $N_{\text{disk}} = 0.36^{+0.13}_{-0.10} \text{ km}^2$ corresponds to an apparent inner radius $r_{\text{in}} = (8, 300^{+1,600}_{-1,300}) (\cos\theta)^{-1/2} \text{ km}$. We find an even better agreement with a power-law model (Figure 10), with $\text{Cstat} = 76$ (32 + 44 from the 2009 and 2023 data points, respectively) over 98 dof. In this case, $N_{\text{H,int}} = 1.0^{+0.7}_{-0.5} \times 10^{21} \text{ cm}^{-2}$ and $\Gamma = 3.83^{+0.54}_{-0.46}$. In summary, we cannot rule out the possibility that HLX-1 was in the same spectral state in 2009 and 2023.

7. Origin of the Optical Emission

The point-like optical/UV counterpart (Section 5) is too bright ($M_{\text{V}} \approx -11 \text{ mag}$) to be an individual star. Given its relatively blue optical colors, it could be a young massive star cluster in the halo of NGC 6099 (a very atypical situation for an elliptical galaxy); or it could be dominated by reprocessed emission from the X-ray source; or it could be a background AGN/quasar. More complicated scenarios are also possible, such as blue/UV emission from X-ray reprocessing in the accretion flow and red/IR emission from a host old star cluster.

Table 5

Optical/X-Ray SED from the 2022–2023 Data, Fitted with an X-Ray Comptonization Model Plus an Independent Optical/UV Blackbody: $\text{TBabs} \times \text{TBabs}_{\text{int}} \times (\text{simpl} \times \text{diskbb}) + \text{redden} \times \text{redden}_{\text{int}} \times \text{bbodyrad}[+0.04 \times \text{TBabs} \times \text{TBabs}_{\text{gal}} \times \text{apec}_{\text{gal}}]$

Component	Parameter	Value	Unit
$\text{redden}_{\text{int}}$	$E(B - V)$	$0.36^{+0.18}_{-0.12}$	mag
$\text{TBabs}_{\text{int}}$	$N_{\text{H,int}}$	$0.17^{+0.05}_{-0.10}$	10^{22} cm^{-2}
simpl	Γ	$3.6^{+0.9}_{-0.3}$...
	FracSctr	$0.18^{+0.79}_{-0.07}$...
diskbb	UpSc	[0.0]	...
	kT_{in}	$0.07^{+0.01}_{-0.04}$	keV
bbrad	$N_{\text{disk}}^{\text{a}}$	709^{+1110}_{-432}	km^2
	T_{bb}	$2.2^{+3.2}_{-0.6}$	10^4 K
$\text{TBabs}_{\text{gal}}$	N_{bb}	$4.1^{+1.4}_{-2.2}$	10^8 km^2
	$N_{\text{H,gal}}$	[0.57]	10^{22} cm^{-2}
apecgal	kT	[0.37]	keV
	$N_{\text{apec}}^{\text{b}}$	[6.85]	See notes
χ^2/dof		39/50	
$R_{\text{in}}\sqrt{\cos\theta}$		44^{+27}_{-16}	10^9 cm
R_{bb}		$2.83^{+0.51}_{-0.78}$	10^{13} cm
F_{X}^{c}		$1.4^{+0.1}_{-0.1} \times 10^{-14}$	$\text{erg cm}^{-2} \text{ s}^{-1}$
L_{X}^{d}		$1.6^{+0.2}_{-0.2} \times 10^{41}$	erg s^{-1}

Notes. The last term accounts for the contamination of thermal emission from the host galaxy NGC 6099; we did not include this term in the flux and luminosity of HLX-1. The errors are 90% confidence limits for one interesting parameter. The X-ray line-of-sight absorption is $N_{\text{H}} \equiv 4.16 \times 10^{20} \text{ cm}^{-2}$; the line-of-sight reddening is $E(B - V) \equiv 0.05 \text{ mag}$.

^a The disk normalization N_{disk} and inner-disk radius R_{in} are related by $R_{\text{in}}\sqrt{\cos\theta} \approx 1.19\sqrt{N_{\text{disk}}}d_{10}$, where $d_{10} \approx 13,900$ is the distance in units of 10 kpc.

^b N_{apec} is defined here as 10^{-5} times the XSPEC *apec* model normalization.

^c Absorbed flux in the 0.3–10 keV band.

^d Unabsorbed isotropic luminosity in the 0.3–10 keV band.

This uncertainty is reminiscent of the debate about the interpretation of the optical counterpart of the IMBH candidate ESO 243-49 HLX-1, initially interpreted as a young star cluster (S. A. Farrell et al. 2012) and then attributed (at least for the blue/UV component) to reprocessed disk emission (R. Soria et al. 2012, 2017), because its brightness varied together with the X-ray flux. In the case of HLX-1, we do not have a spectroscopic optical redshift, to test the background AGN scenario, nor do we have multiple-epoch observations to test the correlation with X-ray luminosity. For now, we can constrain the X-ray/optical flux ratio to determine which of the three alternatives (IMBH disk, star cluster, or AGN) is more likely. We do not have contemporaneous optical and X-ray observations; our CFHT data were taken in 2022 August, the HST data in 2023 September, and the closest X-ray observation is from 2023 August. There is only marginal evidence of a small optical variability between 2022 and 2023, based on the comparison between the extinction-corrected CFHT measurement of $m_{g,\text{AB}} = (24.41 \pm 0.16) \text{ mag}$ and the HST value of $m_{\text{F475W,AB}} \approx g' \approx g = (24.62 \pm 0.05) \text{ mag}$ (Section 5). In any case, the change is small enough that we can use both the 2022 and 2023 optical data together, for a comparison with the 2023 X-ray data.

To model the broadband SED, we combined the 2023 XMM-Newton/EPIC measurements with six optical/UV data

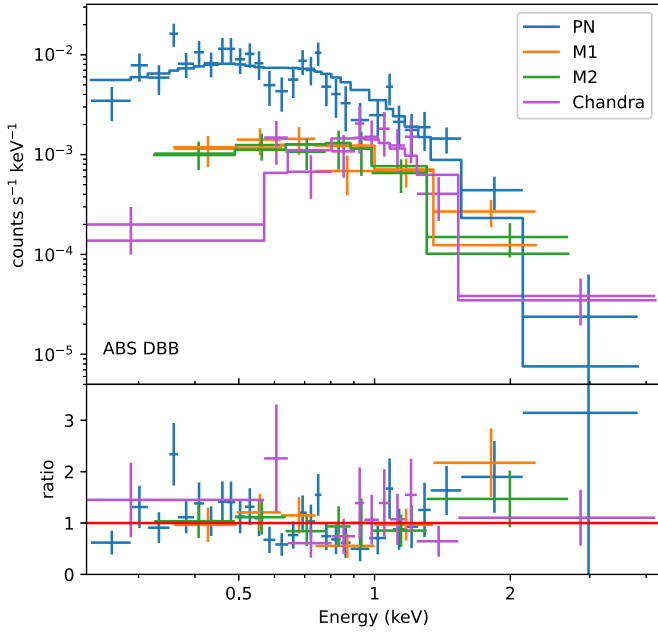


Figure 9. Simultaneous fit of the 2009 Chandra spectrum (orchid data points and model fit) and 2023 XMM-Newton/EPIC spectrum (blue = pn; orange = MOS1; and green = MOS2) with an absorbed disk blackbody model. Top: data points and best-fitting model. Bottom: data/model ratios. For all four spectra, the data have been grouped to a minimum signal-to-noise ratio of 2, for plotting purposes only.

points (u , g , r from CFHT/Megacam; F300X, F475W, and F814W from HST/WFC3). We used the FTOOLS task `ftflx2xsp` to convert each of the six optical/UV flux measurements into *pha* format, suitable for XSPEC modeling. We tried two models: one in which the optical/UV data points are tied to the soft X-ray emission (`diskir`) and one in which the X-ray and optical bands are uncorrelated—in the latter case, we used the `simpl` Comptonization model for the X-ray emission and a blackbody model for the optical data points.

7.1. Irradiated Accretion Disk

To reduce the number of simultaneously free parameters, we fitted the SED with `diskir` in three steps.

First (as reported in Section 6.3), we included only the X-ray data points, left the Comptonization fraction (L_c/L_d), photon index (Γ), peak disk temperature (kT_{in}), disk normalization (proportional to r_{in}^2), and intrinsic absorption column ($N_{H,in}$) as free parameters, and froze the (unconstrained) electron temperature (T_e), irradiation radius (r_{irr}), fraction of luminosity in the Compton tail thermalized in the inner disk (f_{in}), reprocessing factor (f_{out}), and outer-disk size ($\log(r_{out}/r_{in})$) (the latter two parameters are unconstrained without optical/UV data). As in all other cases, we also included the small fixed contamination component from the thermal plasma emission of NGC 6099.

In the second step, we added the six optical/UV data points. We froze the X-ray parameters at their best-fitting value, thawed f_{out} and $\log(r_{out}/r_{in})$, and included two optical/UV extinction components (`reddden` \times `redddenint`), one for the line-of-sight reddening (fixed at $E(B - V) = 0.05$ mag) and the other for the intrinsic reddening (keeping in mind that X-ray photons and optical photons come to us along different lines of sight and may see different amounts of scattering and absorption). Thus, in the second step, the fitting procedure

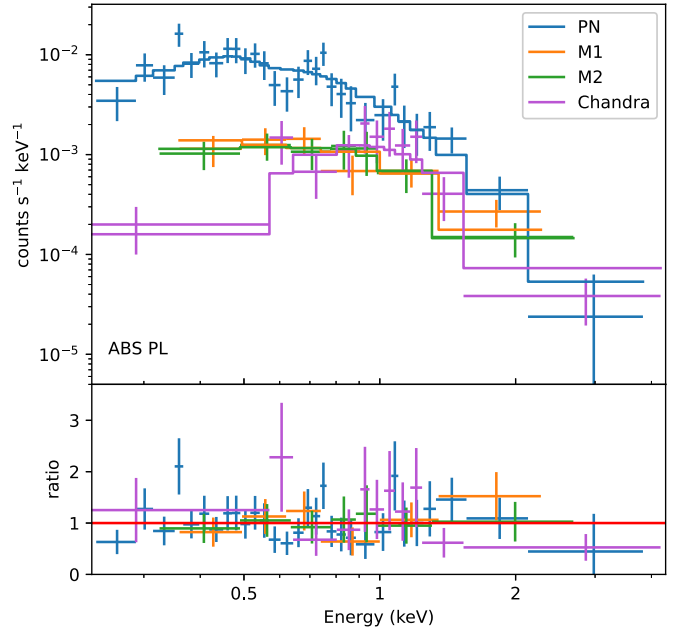


Figure 10. The same as Figure 9 but for an absorbed power-law model.

has three free parameters available for six optical/UV data points.

Finally, we thawed the X-ray parameters again and used the `steppar` command in XSPEC around the previous best-fit values, to check whether the inclusion of the optical/UV part of the spectrum leads to small changes in the best-fitting values of the X-ray parameters. We found that such changes are negligible—that is, the values of the X-ray parameters in the final SED model remain within the error range of the initial X-ray-only fit.

The final model (Figure 11 and Table 4) has $\chi^2 = 41/50$ dof. The best-fitting parameters related to the X-ray data have already been mentioned in Section 6.3. The addition of the optical data enables us to determine three more parameters: the outer-disk radius R_{out} , the X-ray-reprocessing fraction f_{out} , and the intrinsic optical reddening $E(B - V)$. The outer-disk radius is $R_{out} = (6 \pm 4) \times 10^{13} (\cos \theta)^{-1/2}$ cm. The reprocessing fraction of $f_{out} \approx$ a few percent is consistent with the range of values observed in ULXs (F. Grisé et al. 2012; A. D. Sutton et al. 2014; Y. Qiu & H. Feng 2021) and in the IMBH candidate ESO 243-49 HLX-1 (R. Soria et al. 2017). Finally, the best-fitting intrinsic optical reddening is low, consistent with the line of sight only.

7.2. Stellar Cluster

Instead of a single irradiated disk model for the optical-to-X-ray data, we tried fitting the X-ray and optical data with separate, independent components: a Comptonization model (`simpl` \times `diskbb` and a blackbody model (`bbbodyrad`), respectively. The best-fitting model (Figure 11 and Table 5) has $\chi^2 = 39/50$ dof, with an unabsorbed 0.3–10 keV luminosity $L_X = (1.6 \pm 0.2) \times 10^{41}$ erg s $^{-1}$. The best-fitting parameters for the X-ray component are those already mentioned in Section 6.3. The best-fitting temperature of the optical/UV blackbody component is $kT_{bb} \approx 1.9$ eV (i.e., $T_{bb} \approx 21,800$ K), consistent with a young stellar population dominated by OB stars. The best-fitting blackbody radius is $R_{bb} = (2.8_{-0.9}^{+0.5}) \times 10^{13}$ cm.

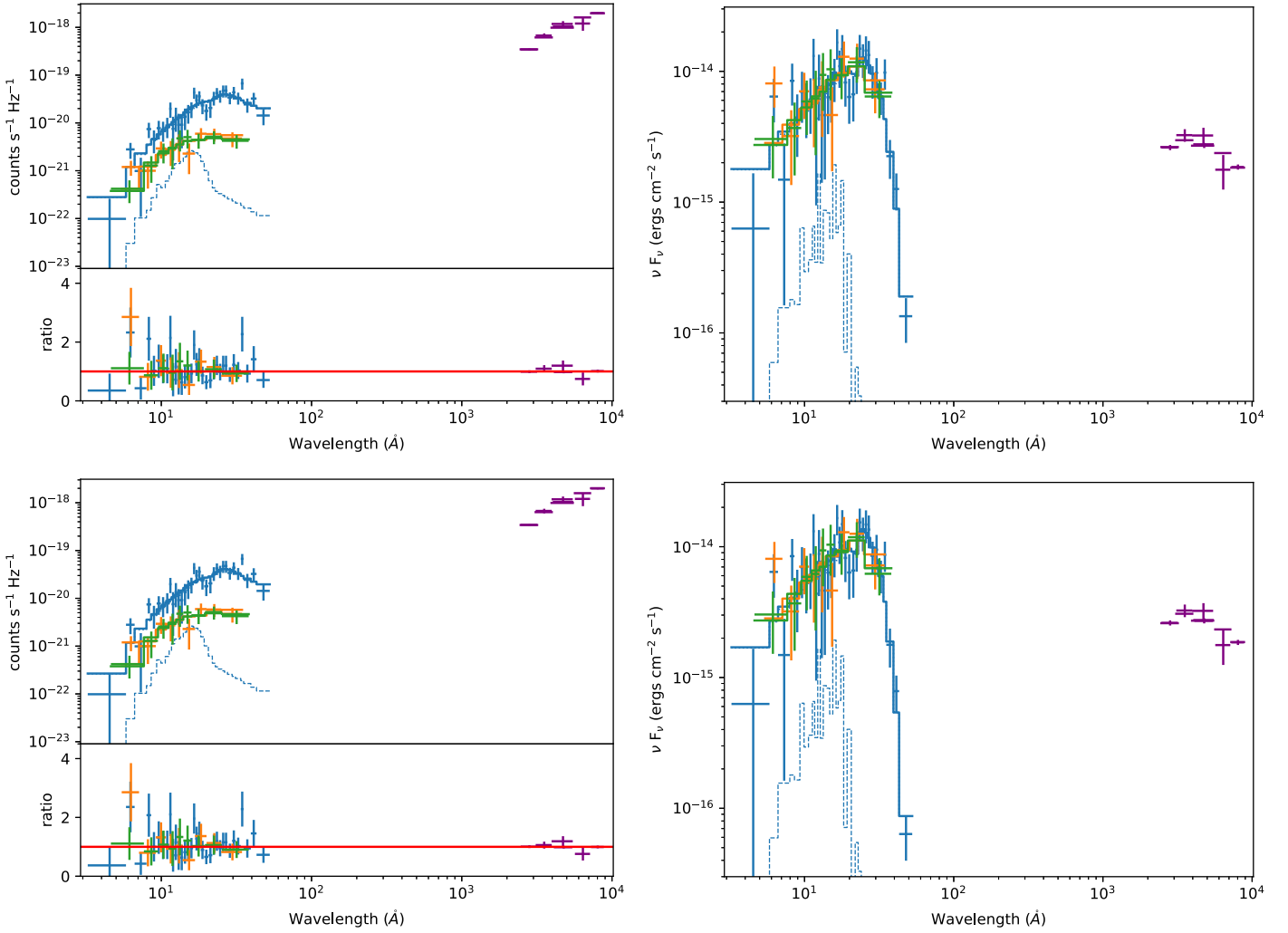


Figure 11. Combined X-ray (2023) and optical (2022–2023) data, fitted with alternative models. The colors are: blue for EPIC-pn; orange for EPIC-MOS1; green for EPIC-MOS2; and purple for CFHT and HST. For the EPIC-pn data, we also plotted the modeled contribution from the contaminating X-ray emission of NGC 6099 (dashed line). The left column contains the SEDs with the data/model ratios plotted underneath; the right column shows the unfolded spectra. The first row illustrates an irradiated accretion-disk model (Section 7.1 and Table 4); the second row illustrates a combined model of a Comptonized X-ray disk plus optical/UV blackbody (Section 7.2 and Table 5).

In summary, both the model in which the optical emission comes from an X-ray-irradiated disk and the model in which it comes from a stand-alone blackbody component lead to equally acceptable fits. Not surprisingly, the same result is obtained also with a combination of disk and blackbody, for example a `diskirr` model with negligible X-ray reprocessing ($f \approx 0$) plus a blackbody. The only significant difference between the two types of models is that an independent blackbody allows for a larger range of optical reddening, because the temperature and normalization of the optical/UV component are not linked to the X-ray component. For low reddening (total $E(B - V) \lesssim 0.1$ mag), the bolometric luminosity of the optical/UV component at the distance of NGC 6099 is $\sim 10^{40}$ erg s $^{-1}$. For higher reddening, $E(B - V) \approx 0.3$ – 0.6 mag (Table 5), the intrinsic luminosity of the optical/UV emission can be as high as $\sim 10^{41}$ erg s $^{-1}$.

8. Discussion

The observed properties of HLX-1 make it an unusual and intriguing source, difficult to categorize into ordinary classes of accreting compact objects. All three X-ray detections (Chandra

in 2009 and XMM-Newton in 2012 and 2023) show a soft, likely thermal spectrum. However, the spectra are not consistent with the “canonical” high/soft state with constant normalization (a standard disk truncated at the innermost stable circular orbit) and $L_{\text{disk}} \propto T_{\text{in}}^4$. The uncertainty in the interpretation of the inner-disk radius across different epochs and for different models, together with the lack of optical redshift measurements and the lack of simultaneous optical/X-ray observations, make it more difficult to distinguish between IMBH scenarios at the distance of NGC 6099 and a background AGN. Nonetheless, we can assess the pros and cons of several alternative scenarios.

8.1. Canonical State Transitions of an IMBH?

In this scenario, HLX-1 was in a canonical sub-Eddington state in 2009, a super-Eddington state in 2012, and back to a sub-Eddington state in 2023. This requires an IMBH accretor with a mass $\sim 10^3$ – $10^4 M_{\odot}$. We showed (Section 6.4) that the 2009 and 2023 spectra are consistent with the same state and suggest a characteristic radius $R_{\text{in}} \sqrt{\cos \theta} \approx 10,000$ km. If R_{in} corresponds to the innermost stable circular orbit R_{isco} , the BH

mass is a few $\times 10^3 M_\odot$ (with the exact value depending on the unknown spin parameter), self-consistent with the luminosity argument ($L_{\text{Edd}} \sim \text{a few} \times 10^{41} \text{ erg s}^{-1}$).

Standard disk instability models predict that below a threshold accretion rate (or, equivalently, for an outer disk larger than a minimum radius), the outer accretion disk becomes mostly neutral and may give rise to thermal–viscous instability cycles (e.g., A. R. King et al. 1997; L. Burderi et al. 1998; G. Dubus et al. 1999, 2001; J.-P. Lasota 2001; V. Kalogera et al. 2004). Such cycles appear observationally as X-ray state transitions. To explore this scenario, let us assume that the optical emission of HLX-1 comes mostly from a large accretion disk. At the large outer radius inferred from the `diskir` model fit, $R_{\text{out}} = (6 \pm 4) \times 10^{13} (\cos \theta)^{-1/2} \text{ cm}$ (Section 7.1), the source of optical emission is mostly X-ray irradiation and reprocessing, rather than viscous dissipation. Based on the irradiation temperature profiles calculated by G. Dubus et al. (1999), the critical accretion rate below which the transient behavior occurs is

$$\dot{M}_{\text{cr}} \approx 3.2 \times 10^{21} \left(\frac{M}{10^4 M_\odot} \right)^{-0.4} \left(\frac{R_{\text{out}}}{6 \times 10^{13} \text{ cm}} \right)^{2.1} \text{ g s}^{-1}. \quad (1)$$

The accretion rate corresponding to the luminosity inferred in 2009 and 2023 is $\dot{M} \approx L_X / (0.1c^2) \approx 10^{21} \text{ g s}^{-1}$. Thus, it is possible that such an accretion rate is not sufficient to keep hydrogen fully ionized in the outer disk, giving rise instead to transient cycles. It is difficult to assess the plausibility of this scenario, because it is not common behavior for stellar-mass accretors (let alone putative IMBH accretors) to switch between a canonical high/soft state and a highly super-Eddington state without transiting through other states. Future X-ray observations of HLX-1—for example, in the low/hard state—are needed to constrain and support or refute this scenario. However, we may not have a chance to see such a transition to the low/hard state happen in our lifetime, because the characteristic outburst decay timescale (i.e., the time required for the outside-in propagation of a cooling front) for a disk radius of $6 \times 10^{13} \text{ cm}$ and a BH mass of $10^4 M_\odot$ is $\approx 300 \text{ yr}$ (J. M. Hameury & J. P. Lasota 2020).

An additional issue to consider is whether a single donor star can steadily feed the IMBH accretion disk at the required rate, via Roche-lobe overflow, without being tidally disrupted. Assuming a mass ratio $q \sim 10^{-3}$ between donor star and IMBH, an accretion-disk radius of $R_{\text{out}} \approx 6 \times 10^{13} \text{ cm}$ suggests a binary separation $a \approx 10^{14} \text{ cm}$ and a Roche-lobe radius $R_2 \approx 70R_\odot$ for the donor star (B. Paczynski 1977; P. P. Eggleton 1983; J. Frank et al. 2002). Thus, in principle, there are several types of young (blue/yellow supergiant) or old (red giant) stars that can fill their Roche lobe in a circular orbit around an IMBH. The expected mass-transfer rate depends on how the internal structure of the donor star responds to rapid mass loss and how its orbit widens or shrinks under the combined effect of angular momentum redistribution and gravitational decay between the star and the IMBH (R. F. Webbink 1985; M. S. Hjellming & R. F. Webbink 1987; H. Ge et al. 2010; L. Dai & R. Blandford 2013; L. Dai et al. 2013). Further investigation of this issue is beyond the scope of this paper.

An alternative scenario we shall only briefly mention here is that the IMBH may instead be recurrently fed at periastron by a donor star on an eccentric orbit, possibly even undergoing partial tidal disruption at each periastron passage (J.-H. Chen & R.-F. Shen 2021; C. J. Nixon et al. 2021; M. Cufari et al. 2022). In this scenario, the 2012 observation was taken shortly after a periastron flare, while the 2009 and 2023 observations were taken later, in a flare decline phase. A similar scenario has been proposed and investigated to explain the X-ray outbursts in the other strong IMBH candidate ESO 243-49 HLX-1 (O. Godet et al. 2014; E. van der Helm et al. 2016) and in some galactic nuclear transients (S. Campana et al. 2015; Z. Liu et al. 2023).

Finally, regardless of the physical reason for the outbursts, if the accreting IMBH exceeds its Eddington luminosity, we expect the fitted radius of the thermal X-ray emission to become larger than the innermost stable circular orbit. This is because in supercritical accretion, such large radii correspond to the spherization radius (N. I. Shakura & R. A. Sunyaev 1973; J. Poutanen et al. 2007), $R_{\text{sph}} \propto \dot{m} R_{\text{in}}$, the radius at which the disk becomes geometrically thick, advective, and from where fast outflows are launched. The situation may be more complicated, if the thermal continuum is not the optically thick emission from a section of the disk surface but instead emission from the scattering photosphere of the wind—for example, the walls of a polar funnel; this is still an unsolved question even in nearby ULXs with much better observational coverage (e.g., R. Narayan et al. 2017; D. J. Walton et al. 2020, 2024; A. Gurpide et al. 2021; A. Robba et al. 2021; F. Barra et al. 2022, 2024).

8.2. A Full TDE with Delayed X-Ray Peak?

In this scenario, the similar X-ray flux levels and soft spectra seen in 2009 and 2023 (before and after the 2012 peak) are only a coincidence and do not correspond to similar intrinsic luminosities and spectral states in the two epochs. The 2009 spectrum corresponds to the early rise of the TDE emission, the 2012 spectrum was taken near the peak, and the 2023 data come from the decline phase.

After two decades of intense theoretical and observational studies, it is still actively debated what fraction of TDE emission originates from viscous dissipation and accretion onto the BH and what fraction originates from shocks (stream–stream collisions) during the debris circularization phase (e.g., G. Lodato & E. M. Rossi 2011; T. Piran et al. 2015; B. D. Metzger & N. C. Stone 2016; B. D. Metzger 2022; E. Steinberg & N. C. Stone 2024).

The first possibility is that in 2009, HLX-1 was in the initial super-Eddington accretion phase, and the accretion rate has monotonically declined since then. The main feature of a super-Eddington phase is the launching of thick outflows, which downscatter and reprocess the X-ray photons emitted close to the compact object (e.g., G. Lodato & E. M. Rossi 2011; B. D. Metzger & N. C. Stone 2016; N. Roth et al. 2016; L. Dai et al. 2018; D.-F. Bu et al. 2022; B. D. Metzger 2022; L. L. Thomsen et al. 2022). The initial spectrum peaks in the optical/UV; soft X-rays rise later, after the super-Eddington outflow has stopped and the reprocessing envelope has cooled or shrunk (B. D. Metzger & N. C. Stone 2016; N. Roth et al. 2016; J.-H. Chen & R.-F. Shen 2018; T. Wevers et al. 2019; B. D. Metzger 2022). In particular, for an initially super-Eddington IMBH TDE, the timescale t_{Edd} on which the

fallback rate declines below the Eddington rate is $t_{\text{Edd}} \simeq 14 \eta_{0.1}^{3/5} M_4^{-2/5} r_*^{3/5} m_*^{1/5}$ yr (J.-H. Chen & R.-F. Shen 2018), where $\eta_{0.1} \equiv \eta/0.1$ is the radiative efficiency, M_4 is the BH mass in units of $10^4 M_\odot$, and r_* and m_* are the disrupted star’s radius and mass in solar units, respectively. Therefore, the initial optically bright, X-ray-faint phase may last for several years in IMBH TDEs (J.-H. Chen & R.-F. Shen 2018; V. L. Tang et al. 2024). If this is the correct timeline of events for HLX-1, it implies that in 2009, at least 99% of the emitted X-ray photons were blocked by the reprocessing envelope, and, as a result, the optical/UV luminosity should have been at least as high as the X-ray luminosity in 2012 (a few times 10^{42} erg s $^{-1}$), corresponding to a visual magnitude $m_{g,AB} < 19$ mag. Such optical brightening should have been detectable by the main widefield transient surveys active circa 2009. We inspected 34 *R*-band images (exposure times of 60 s each) taken by the Palomar Transient Factory (PTF; N. M. Law et al. 2009; A. Rau et al. 2009) from the 48 inch Samuel Oschin Telescope between 2009 May and 2010 August.²¹ We did not find any source at the location of HLX-1 in any frame, down to an individual-frame detection limit of $m_{R,AB} \approx 20.5$ mag. We used the IRAF task `imcombine` to build separate stacked images of all the 2009 and 2010 observations, and found that HLX-1 was not detected in either year, down to a limit of $m_{R,AB} \approx 21.5$ mag. Further PTF observations from the 48 inch telescope were also taken in 2013 February (five 60 s exposures), March (41 exposures), April (47 exposures), and May (46 exposures). We also built separate stacked images for those four epochs and verified once again a nondetection, with an upper limit of $m_{R,AB} \approx 21$ mag in 2013 February and $m_{R,AB} \approx 21.5$ mag for the other three months. This suggests that shortly after the 2012 X-ray outburst, there was no bright optical/UV envelope either. We conclude that the super-Eddington optical/UV reprocessing scenario is not supported by the optical data.

The second possibility is that the bolometric luminosity of HLX-1 was sub-Eddington and much lower than in 2012 (consistent with the lack of a bright optical counterpart). In this case, the X-ray emission in 2009 was due to shocks in the self-colliding stream or from stream compression near the pericenter, during the initial circularization phase of the TDE, before disk formation (T. Piran et al. 2015; T. Wevers et al. 2019; J.-H. Chen & R.-F. Shen 2021; X.-L. Liu et al. 2022; X. Huang et al. 2024; E. Steinberg & N. C. Stone 2024). Instead, the emission seen in 2012 and 2023 was from viscous dissipation and accretion, after debris circularization. This scenario is more plausible if there is a substantial time delay (months or years) between stellar disruption and disk formation. One of the parameters affecting the timescale for debris circularization is the amount of apsidal precession of the stream, which decreases at lower BH masses (L. Dai et al. 2015; J. Guillochon & E. Ramirez-Ruiz 2015; H. Shiokawa et al. 2015; K. Hayasaki et al. 2016; C. Bonnerot et al. 2017; X.-L. Liu et al. 2022). For example, the candidate TDE ASASSN-15oi had a slow-rising phase in the soft X-ray band for about 1 yr (S. Gezari et al. 2017; T. W. S. Holoien et al. 2018), which may correspond to a slow circularization phase around a relatively light BH. The recently discovered soft X-ray transient EP240222a (C.-C. Jin et al. 2025) may have had a 3 yr circularization phase, consistent with an IMBH with $M \sim 10^5 M_\odot$. In summary, HLX-1 may be a good representative

of the class of IMBH TDEs in globular clusters, in which faint precursor X-ray emission from stream–stream collisions occurs months or years before the peak of the accretion-powered emission.

8.3. A Background Changing-look, Supersoft AGN?

As anticipated in the outline of our source selection (Section 2.1), the two main X-ray properties (flux variability by 2 orders of magnitude and extreme softness), by themselves, are not fireproof evidence of a high-state IMBH. We have already mentioned that some changing-look AGNs (S. Komossa & D. Grupe 2023) show dramatic X-ray luminosity variations over a few years. A good example is 1ES 1927+654 (L. C. Gallo et al. 2013; C. Ricci et al. 2020; R. Li et al. 2022, 2024; M. Masterson et al. 2022; X. Cao et al. 2023; $d \approx 87$ Mpc, $z \approx 0.019$), which is believed to have reached its Eddington limit at $L_X \approx 10^{44}$ erg s $^{-1}$, with a soft thermal spectrum and peak temperature $kT_{\text{in}} \approx 0.15\text{--}0.20$ keV, during its well-monitored 2019–2020 outburst. The spiral galaxy IC 3599 ($d \approx 93$ Mpc, $z \approx 0.021$) is another good example of a changing-look AGN (S. Campana et al. 2015; D. Grupe et al. 2015, 2024): it has shown at least two outbursts (1990 and 2010), reaching peak luminosities of a few $\times 10^{43}$ erg s $^{-1}$, from a baseline luminosity of a few $\times 10^{40}$ erg s $^{-1}$. IC 3599 has also shown soft spectra at all epochs, well fitted by a blackbody with $kT_{\text{bb}} \approx 0.1$ keV or a steep power-law spectrum with $\Gamma > 3$ (S. Campana et al. 2015). A sample of 60 nuclear sources with a supersoft spectrum (power-law photon index $\Gamma \gtrsim 3$ and/or a dominant blackbody component at $kT_{\text{bb}} \sim 0.1\text{--}0.2$ keV) was collected and discussed by A. Sacchi et al. (2023) from the 4XMM-DR9 catalog.

One possible explanation for a changing-look, soft-spectrum AGN is a TDE or partial TDE (S. Campana et al. 2015; C. Ricci et al. 2020; J.-H. Chen & R.-F. Shen 2021; C. J. Nixon et al. 2021; M. Cufari et al. 2022) on a previously active AGN (that is, with a pre-existing accretion disk). In other cases, such as the supersoft (pure thermal spectrum with $kT_{\text{bb}} \approx 0.2$ keV) Seyfert 2 nucleus 2XMM J123103.2+110648 (Y. Terashima et al. 2012; D. Lin et al. 2013), persistent but highly variable activity over many years suggests that it is not a TDE. Explaining the physics of changing-look and supersoft AGNs is beyond the scope of this work. What matters here is whether we might have misidentified one such (background) AGN for an off-nuclear source in NGC 6099. To answer this question, we need to look at its optical appearance.

In the 2022–2023 data sets, HLX-1 has a characteristic observed 0.3–10 keV flux over *u*-band flux ≈ 10 (Tables 2 and 3); for the *r* band, the X-ray over optical flux ratio is ≈ 20 . Such values are low enough to be consistent with AGNs and IMBHs. By comparison, the extreme changing-look AGN 1ES 1927+654 has $f_{\text{XO}} \approx 10$ from pre-outburst XMM-Newton observations at $L_X \approx 10^{43}$ erg s $^{-1}$ (L. C. Gallo et al. 2013) and Pan-STARRS *i*-band images. The main constraint comes instead from the point-like, faint appearance of the optical counterpart.

The optical counterpart of 1ES 1927+654 (including only the host galaxy contribution) would look as faint as the optical counterpart of HLX-1 only if that galaxy were located at a luminosity distance 40 times higher than its real distance (R. Li et al. 2022, 2024)—that is, ≈ 3.5 Gpc ($z \approx 0.58$).²² If HLX-1 were a changing-look AGN at that distance, it would have had

²¹ Available from <https://irsa.ipac.caltech.edu/applications/ptf>.

²² For all distance and redshift calculations in this paragraph and the following two, we used Ned Wright’s Cosmology Calculator (E. L. Wright 2006).

an X-ray luminosity of $L_X \approx 2 \times 10^{45} \text{ erg s}^{-1}$ in 2012 and $L_X \approx 2 \times 10^{43} \text{ erg s}^{-1}$ in 2009 and 2023, which is still within the range of plausible Seyfert luminosities. We want to ascertain whether at such a distance, the host galaxy would look point-like or extended. For this test, we take the V -band surface brightness profile for 1ES 1927+654 measured by R. Li et al. (2022; their Figure 1); we neglect K corrections and assume for simplicity that the surface brightness scales as $(1+z)^{-4}$. We then estimate the R_{25} radius at which the observed V -band surface brightness $\mu_V = 25 \text{ mag arcsec}^{-2}$ for a galaxy identical to 1ES 1927+654 but located at $z \approx 0.58$. We obtain $R_{25} \approx 0''.5$. Therefore, the stellar disk emission of such a galaxy would be resolvable in HST images even at that redshift.

Let us consider instead the possibility that HLX-1 is a background AGN hosted by a dwarf galaxy like the dwarf Seyfert 1 galaxy POX 52 (A. J. Barth et al. 2004; C. E. Thornton et al. 2008), located at a luminosity distance of 98 Mpc ($z = 0.0218$). POX 52 would need to be located 30 times farther away, at $z \approx 0.50$ (luminosity distance $\approx 2.9 \text{ Gpc}$), to look as faint as our observed optical source. At that distance, we would measure $R_{25} \approx 0''.3$; thus, even in this case, it would look extended in HST.

Finally, the observed X-ray flux itself constrains the possible distance range of HLX-1 in the background AGN scenario. A distance higher than $z \approx 1.3$ is very unlikely, because it would push its rest-frame peak X-ray luminosity above $10^{46} \text{ erg s}^{-1}$, an approximate upper limit for the X-ray luminosity of AGNs (J. Singal et al. 2022). At that redshift, the upper limit of $0''.15$ to the optical size of HLX-1 (Section 5) corresponds to $\approx 1.3 \text{ kpc}$.

In summary, the point-like appearance and optical faintness of HLX-1 are more consistent with the IMBH scenario in a globular cluster or ultracompact dwarf (UCD) in the NGC 6098/6099 group than a background Seyfert galaxy.

8.4. Host Star Cluster or Irradiated Disk?

Let us assume now that our source is indeed near NGC 6099. Then, its optical counterpart is either coming entirely from a young star cluster, or it is a mix of the (bluer) contribution from an accretion disk and a (redder) contribution from the stellar population in the star cluster.

If all the optical emission comes from the star cluster, the observed blue colors require a young stellar population. We used the population synthesis code STARBURST99 (C. Leitherer et al. 1999, 2014), with the Geneva evolutionary tracks (S. Ekström et al. 2012), to quantify the range of acceptable ages and masses, at different metallicities. From the optical brightness and colors measured from the CFHT and HST data (Section 5), corrected for line-of-sight Galactic reddening, and assuming impulsive star formation, we obtain an age of $\approx 6\text{--}8 \text{ Myr}$ and stellar mass $M_* \approx 4 \times 10^4 M_\odot$ at solar metallicity ($Z = 0.014$) or an age of $\approx 20\text{--}30 \text{ Myr}$ and stellar mass $M_* \approx 2.4 \times 10^5 M_\odot$ at very low metallicity ($Z = 0.002$). Ages younger than $\approx 6 \text{ Myr}$ are ruled out by the moderately red $V - I$ color ($V - I \approx (0.5 \pm 0.2) \text{ mag}$, Section 5), which points to the minimum age at which the most massive surviving stars of the cluster evolve to the red supergiant stage instead of dying as blue stars. Instead, if we include an intrinsic reddening $E(B - V) \approx 0.3\text{--}0.6 \text{ mag}$ (Table 5), we can explain the optical/UV emission with a young stellar population of mass $\approx 10^5 M_\odot$ and ages $\lesssim 5 \text{ Myr}$.

The young cluster scenario faces several challenges. IMBHs are indeed predicted to form in the cores of young clusters via core collapse and stellar collisions, on timescales of a few megayears (S. F. Portegies Zwart & S. L. W. McMillan 2002; M. C. Miller & E. J. M. Colbert 2004; M. Freitag et al. 2006). However, numerical simulations by U. N. Di Carlo et al. (2021) with the MOBSE population synthesis code (M. Mapelli et al. 2017) suggest that clusters with stellar masses up to $3 \times 10^4 M_\odot$ (similar to our solar-metallicity case) do not form IMBHs more massive than $\approx 500 M_\odot$, insufficient to explain the observed luminosity of HLX-1. Moreover, there is no sign of recent star formation (for example, other young star clusters) in the halo of NGC 6099. We cannot exclude that the young star cluster with its central IMBH came from a gas-rich satellite dwarf, accreted and disrupted by NGC 6099; however, we do not see tidal tails or other signatures of such a recent event.

The second possibility is that the bluer component of the optical emission comes from the X-ray-irradiated disk or, more generally, the irradiated accretion inflow/outflow, and the host stellar cluster contains only an old red population (much fainter for the same total stellar mass). For example, with STARBURST99, we find that an old globular cluster or UCD with an age of $\approx 10 \text{ Gyr}$ is consistent with the observed I -band luminosity (and obviously also with the brightness measured in bluer bands) for a stellar mass up to $\approx 2 \times 10^7 M_\odot$. From the relation between the central BH mass and stellar mass valid for UCDs and stripped nuclear star clusters (A. W. Graham & N. Sahu 2023; R. J. Mayes et al. 2024), a stellar system of this mass can harbor a BH of up to $\sim 10^6 M_\odot$. Even a cluster with a much lower stellar mass $\approx 10^6 M_\odot$ may harbor an IMBH up to $\sim 10^4 M_\odot$ (as may be the case for the Galactic globular cluster Omega Cen: M. Häberle et al. 2024), sufficient to explain the X-ray luminosity of our source. An old star cluster also implies that the only plausible feeding mechanism is tidal stripping or disruption of a low-mass star.

The apparent optical radius of $R_{\text{out}} = (6 \pm 4) \times 10^{13} \text{ cm}$ (from our `diskir` model fitting; Section 7.1) is an order of magnitude larger than the predicted circularization radius R_c of a low-mass main-sequence star ($R_c \approx 2R_t \approx 2R_* (M_{\text{BH}}/M_\odot)^{1/3} \sim 40R_\odot \approx 3 \times 10^{12} \text{ cm}$, where R_t is the tidal disruption radius, R_* is the radius of the main-sequence star, and we assumed $M_{\text{BH}} = 10^4 M_\odot$). Large optical radii are a well-known problem in TDE models (e.g., S. Gezari 2021, particularly evident in her Figure 8), where there is a significant discrepancy of 1 and sometimes 2 orders of magnitude between the fitted blackbody radii and the expected circularization radii of the debris disks. This could be due to viscous spreading of the gas in the disk, inward and outward (J. Frank et al. 2002; S. van Velzen et al. 2019). Alternatively, the self-intersection radius of the debris stream should be taken as the most realistic scale for the disk size (S. Gezari 2021). For $M_{\text{BH}} \sim 10^4 M_\odot$, such a radius is \approx a few $\times 10^{13} \text{ cm}$ (L. Dai et al. 2015), consistent with the apparent optical radius in HLX-1.

The relative fraction of optical emission from the irradiated disk (as a function of L_X) and the host star cluster (as a constant) can only be determined from repeated optical observations at different X-ray luminosities and deeper observations in the near-IR. For example, the observed long-term decrease in the blue-band luminosity after X-ray outbursts in the IMBH candidate ESO 243-49 HLX-1 proved that at least the bluer component of the optical emission was coming from

X-ray-irradiated gas in the inflow/outflow (S. A. Farrell et al. 2014; R. Soria et al. 2017).

9. Conclusions

We identified an intriguing high-luminosity, point-like X-ray source from XMM-Newton and Chandra archives. The source satisfies the main selection criteria for an IMBH. It appears to be located at the outskirts of the elliptical galaxy NGC 6099 ($d \approx 139$ Mpc); we call it NGC 6099 HLX-1. The source was detected by Chandra and XMM-Newton at different flux levels in three separate epochs (lower fluxes in 2009 and 2023, with the highest flux in 2012). Its peak luminosity ($L_X \approx$ a few $\times 10^{42}$ erg s^{-1}), combined with a consistently soft X-ray spectrum (an optically thick thermal component with $kT_{in} \approx 0.2$ keV plus a power-law component with photon index $\Gamma \gtrsim 3$), are predicted hallmarks of IMBHs near or above their Eddington limit. The luminosity, time evolution, and spectral properties rule out highly beamed or highly super-Eddington stellar-mass accretors or a young supernova. On the other hand, X-ray variability and soft thermal spectra are also seen in some TDEs and changing-look AGNs.

Moreover, we discovered a blue, point-like optical counterpart in CFHT images; it is also unresolved in follow-up HST images. We estimate a brightness $V_0 = (24.6 \pm 0.2)$ mag (corrected for line-of-sight Galactic reddening), an absolute magnitude $M_{V,Vega} = (-11.1 \pm 0.2)$ mag, and optical colors (corrected for line-of-sight Galactic reddening) $B - V \approx -0.1$ mag, $V - I \approx 0.5$ mag (Vegamag system). The morphology and brightness of the optical counterpart are consistent with a source at the outskirts of NGC 6099, such as a massive star cluster or UCD. We cannot completely rule out a distant background AGN or quasar. However, the latter explanation is more contrived, given the lack of any spatially extended optical feature around the X-ray source. If the AGN was so far away that its host galaxy is undetectable, its rest-frame X-ray luminosity would be unphysically high. There is no evidence of tidal tails or recent star formation in the halo of NGC 6099; thus, we suggest that the IMBH is more likely surrounded by an old or intermediate-age stellar population and that the blue optical emission comes mostly from the X-ray-irradiated accretion flow. A definitive answer for the nature of the optical counterpart will only come from follow-up optical spectroscopy (for the redshift) and photometry (to search for the evolution of the optical colors as a function of X-ray flux).

We discussed alternative interpretations and argued that an IMBH in a compact star cluster, fed by tidal stripping or tidal disruption of a low-mass star, is the simplest explanation consistent with the data at hand. If so, the obvious question is then why the source was already seen in a moderately bright, soft X-ray state in 2009, three years before the 2012 highest-luminosity state. At first sight, the 2009 detection seems to rule out a single TDE. One possible answer is that HLX-1 is fed by tidal stripping of a companion star on an eccentric orbit (partial tidal disruption). This is a model that has been suggested, for example, to explain the repeated X-ray outbursts in the best-known IMBH candidate ESO 243-49 HLX-1. An alternative scenario is that the 2009 observation corresponds to the initial rising phase of a TDE, when the thermal X-ray emission comes mostly from shocked gas in the self-intersecting accretion stream; instead, the 2012 observation (~ 50 – 100 times more luminous, depending on the choice of spectral models) corresponds to the disk accretion phase. Follow-up X-ray

observations will be needed to determine whether the X-ray source is now steadily declining along the expected TDE track (luminosity $\propto t^{-5/3}$), whether and at what luminosity threshold it will switch to the low/hard state (which will constrain the BH mass), or, conversely, whether it will rise again in the future, if the feeding source has not been completely disrupted.

Acknowledgments

We thank the anonymous referee for the detailed corrections and suggestions, which led to a much improved paper. We thank Roberta Amato, Lixin Dai, Hua Feng, Miroslav Filipovic, Andres Gurbide, Chichuan Jin, Mansi Kasliwal, Ji-Feng Liu, Matt Middleton, Rong-Feng Shen, and Beverly Smith for fruitful discussions. Y.C.C. acknowledges hospitality and support from the Osservatorio Astrofisico di Torino during part of this work. R.S. acknowledges hospitality and support from the National Astronomical Observatories of China (University of the Chinese Academy of Sciences, Beijing). This work was performed in part at the Aspen Center for Physics, which is supported by National Science Foundation grant PHY-2210452. This project is supported by the National Science and Technology Council of the Republic of China (Taiwan) through grants 111-2112-M-007-020 and 112-2112-M-007-042. R.S. acknowledges the INAF grant No. 1.05.23.04.04 and also acknowledges the grant No. 12073029 from the National Science Foundation of China. The research of I.C. is supported by the Telescope Data Center, Smithsonian Astrophysical Observatory. This work is partly based on observations obtained with XMM-Newton, an ESA science mission with instruments and contributions directly funded by ESA Member States and NASA. We used data obtained from the Chandra Data Archive and the Chandra Source Catalog, available at doi:[10.25574/cdc.279](https://doi.org/10.25574/cdc.279), and software provided by the Chandra X-ray Center (CXC) in the CIAO application package. This research is also partly based on observations made with the NASA/ESA Hubble Space Telescope, obtained from the Mikulski Archive for Space Telescopes (MAST) at the Space Telescope Science Institute, which is operated by the Association of Universities for Research in Astronomy, Inc., under NASA contract NAS 5-26555. The specific observations analyzed can be accessed via doi:[10.17909/qfmj-4j20](https://doi.org/10.17909/qfmj-4j20). These observations are associated with program ID HST-SNAP-17177. Support for program HST-SNAP-17177 was provided by NASA through a grant from the Space Telescope Science Institute. Furthermore, we used data from the European Space Agency (ESA) mission Gaia (<https://www.cosmos.esa.int/gaia>), processed by the Gaia Data Processing and Analysis Consortium (DPAC, <https://www.cosmos.esa.int/web/gaia/dpac/consortium>). Funding for DPAC has been provided by national institutions, in particular the institutions participating in the Gaia Multilateral Agreement. We used IRAF software for part of the optical analysis: IRAF is distributed by the National Optical Astronomy Observatory, which is operated by the Association of Universities for Research in Astronomy (AURA) under a cooperative agreement with the National Science Foundation. We also used the VizieR data archive and the Aladin sky atlas developed and maintained by CDS, Strasbourg Observatory, France.

Facilities: XMM-Newton, Chandra X-ray Observatory, Neil Gehrels Swift Observatory, Hubble Space Telescope, Canada–France–Hawaii Telescope.

Software: AstroImageJ (K. A. Collins et al. 2017), CIAO (A. Fruscione et al. 2006), Sas (C. Gabriel et al. 2004), Sherpa (P. Freeman et al. 2001; D. Burke et al. 2022; A. Siemiginowska et al. 2024), IRAF (D. Tody 1986, 1993), ftools (J. K. Blackburn 1995; NASA High Energy Astrophysics Science Archive Research Center (Heasarc) 2014), XSPEC (K. A. Arnaud 1996).

ORCID iDs

Yi-Chi Chang  <https://orcid.org/0009-0007-2115-6257>
 Roberto Soria  <https://orcid.org/0000-0002-4622-796X>
 Albert K. H. Kong  <https://orcid.org/0000-0002-5105-344X>
 Alister W. Graham  <https://orcid.org/0000-0002-6496-9414>
 Kirill A. Grishin  <https://orcid.org/0000-0003-3255-7340>
 Igor V. Chilingarian  <https://orcid.org/0000-0002-7924-3253>

References

- Abdullah, M. H., Wilson, G., Klypin, A., et al. 2020, *ApJS*, 246, 2
 Ahumada, R., Allende Prieto, C., Almeida, A., et al. 2020, *ApJS*, 249, 3
 Alam, S., Albareti, F. D., Allende Prieto, C., et al. 2015, *ApJS*, 219, 12
 Alston, W. N., Fabian, A. C., Buisson, D. J. K., et al. 2019, *MNRAS*, 482, 2088
 Arnaud, K. A. 1996, in ASP Conf. Ser. 101, *Astronomical Data Analysis Software and Systems V* (San Francisco, CA: ASP), 17
 Bañados, E., Venemans, B. P., Mazzucchelli, C., et al. 2018, *Natur*, 553, 473
 Barra, F., Pinto, C., Middleton, M., et al. 2024, *A&A*, 682, A94
 Barra, F., Pinto, C., Walton, D. J., et al. 2022, *MNRAS*, 516, 3972
 Barrows, R. S., Mezcua, M., & Comerford, J. M. 2019, *ApJ*, 882, 181
 Barrows, R. S., Mezcua, M., Comerford, J. M., & Stern, D. 2024, *ApJ*, 964, 187
 Barth, A. J., Ho, L. C., Rutledge, R. E., & Sargent, W. L. W. 2004, *ApJ*, 607, 90
 Bellovary, J. M., Governato, F., Quinn, T. R., et al. 2010, *ApJL*, 721, L148
 Bernadich, M. C. I., Schwobe, A. D., Kovlakas, K., Zezas, A., & Traulsen, I. 2022, *A&A*, 659, A188
 Bertin, E., & Arnouts, S. 1996, *A&AS*, 117, 393
 Blackburn, J. K. 1995, in ASP Conf. Ser. 77, *Astronomical Data Analysis Software and Systems IV* (San Francisco, CA: ASP), 367
 Boller, T., Fabian, A. C., Sunyaev, R., et al. 2002, *MNRAS*, 329, L1
 Bonnerot, C., Rossi, E. M., & Lodato, G. 2017, *MNRAS*, 464, 2816
 Bu, D.-F., Qiao, E., Yang, X.-H., et al. 2022, *MNRAS*, 516, 2833
 Burderi, L., King, A. R., & Szuszkiewicz, E. 1998, *ApJ*, 509, 85
 Burke, D., Laurino, O., McLaughlin, W. L., et al. 2022, sherpa/sherpa: Sherpa v4.15.0, Zenodo, doi:10.5281/zenodo.7186379
 Caballero-García, M. D., Papadakis, I. E., Dovčiak, M., et al. 2020, *MNRAS*, 498, 3184
 Campana, S., Mainetti, D., Colpi, M., et al. 2015, *A&A*, 581, A17
 Cao, X., You, B., & Wei, X. 2023, *MNRAS*, 526, 2331
 Cardelli, J. A., Clayton, G. C., & Mathis, J. S. 1989, *ApJ*, 345, 245
 Cash, W. 1979, *ApJ*, 228, 939
 Chen, J.-H., & Shen, R.-F. 2018, *ApJ*, 867, 20
 Chen, J.-H., & Shen, R.-F. 2021, *ApJ*, 914, 69
 Chilingarian, I. V., Katkov, I. Y., Zolotukhin, I. Y., et al. 2018, *ApJ*, 863, 1
 Civano, F., Elvis, M., Brusa, M., et al. 2012, *ApJS*, 201, 30
 Collins, K. A., Kielkopf, J. F., Stassun, K. G., & Hessman, F. V. 2017, *AJ*, 153, 77
 Corral, A., Della Ceca, R., Caccianiga, A., et al. 2011, *A&A*, 530, A42
 Crummy, J., Fabian, A. C., Gallo, L., & Ross, R. R. 2006, *MNRAS*, 365, 1067
 Cufari, M., Coughlin, E. R., & Nixon, C. J. 2022, *ApJL*, 929, L20
 Dai, L., & Blandford, R. 2013, *MNRAS*, 434, 2948
 Dai, L., Blandford, R. D., & Eggleton, P. P. 2013, *MNRAS*, 434, 2940
 Dai, L., McKinney, J. C., & Miller, M. C. 2015, *ApJL*, 812, L39
 Dai, L., McKinney, J. C., Roth, N., Ramirez-Ruiz, E., & Miller, M. C. 2018, *ApJL*, 859, L20
 Dausser, T., Svoboda, J., Scharrel, N., et al. 2012, *MNRAS*, 422, 1914
 Davis, B. L., & Graham, A. W. 2021, *PASA*, 38, e030
 Davis, S. W., & El-Abd, S. 2019, *ApJ*, 874, 23
 Di Carlo, U. N., Mapelli, M., Pasquato, M., et al. 2021, *MNRAS*, 507, 5132
 Di Matteo, T., Ni, Y., Chen, N., et al. 2023, *MNRAS*, 525, 1479
 Dickey, J. M., & Lockman, F. J. 1990, *ARA&A*, 28, 215
 Dobrotka, A., Negoro, H., & Bezák, P. 2024, *A&A*, 692, A94
 Done, C., Davis, S. W., Jin, C., Blaes, O., & Ward, M. 2012, *MNRAS*, 420, 1848
 Dubus, G., Hameury, J. M., & Lasota, J. P. 2001, *A&A*, 373, 251
 Dubus, G., Lasota, J.-P., Hameury, J.-M., & Charles, P. 1999, *MNRAS*, 303, 139
 Duncan, K. J. 2022, *MNRAS*, 512, 3662
 Earnshaw, H. P., Roberts, T. P., Middleton, M. J., Walton, D. J., & Mateos, S. 2019, *MNRAS*, 483, 5554
 Eggleton, P. P. 1983, *ApJ*, 268, 368
 Ekström, S., Georgy, C., Eggenberger, P., et al. 2012, *A&A*, 537, A146
 Elias-Chávez, M., Longinotti, A. L., Krongold, Y., et al. 2024, *MNRAS*, 532, 1564
 Evans, I. N., Evans, J. D., Martínez-Galarza, J. R., et al. 2024, *ApJS*, 274, 22
 Evans, I. N., Primini, F. A., Glotfelty, K. J., et al. 2010, *ApJS*, 189, 37
 Fan, X., Bañados, E., & Simcoe, R. A. 2023, *ARA&A*, 61, 373
 Farrell, S. A., Servillat, M., Gladstone, J. C., et al. 2014, *MNRAS*, 437, 1208
 Farrell, S. A., Servillat, M., Pforr, J., et al. 2012, *ApJL*, 747, L13
 Farrell, S. A., Webb, N. A., Barret, D., Godet, O., & Rodrigues, J. M. 2009, *Natur*, 460, 73
 Fender, R. P., Belloni, T. M., & Gallo, E. 2004, *MNRAS*, 355, 1105
 Feng, H., & Soria, R. 2011, *NewAR*, 55, 166
 Frank, J., King, A., & Raine, D. J. 2002, *Accretion Power in Astrophysics: Third Edition* (Cambridge: Cambridge Univ. Press)
 Freeman, P., Doe, S., & Siemiginowska, A. 2001, *Proc. SPIE*, 4477, 76
 Freitag, M., Gürkan, M. A., & Rasio, F. A. 2006, *MNRAS*, 368, 141
 Fruscione, A., McDowell, J. C., Allen, G. E., et al. 2006, *Proc. SPIE*, 6270, 62701V
 Fürst, F., Walton, D. J., Stern, D., et al. 2017, *ApJ*, 834, 77
 Gabriel, C., Denby, M., Fyfe, D. J., et al. 2004, in ASP Conf. Ser. 314, *Astronomical Data Analysis Software and Systems (ADASS) XIII*, ed. F. Ochsenbein, M. G. Allen, & D. Egret (San Francisco, CA: ASP), 759
 Gaia Collaboration 2022, *yCat*, 1/355
 Gallo, L. C., MacMackin, C., Vasudevan, R., et al. 2013, *MNRAS*, 433, 421
 Gao, Y., Wang, Q. D., Appleton, P. N., & Lucas, R. A. 2003, *ApJL*, 596, L171
 Ge, H., Hjellming, M. S., Webbink, R. F., Chen, X., & Han, Z. 2010, *ApJ*, 717, 724
 Gezari, S. 2021, *ARA&A*, 59, 21
 Gezari, S., Cenko, S. B., & Arcavi, I. 2017, *ApJL*, 851, L47
 Gierliński, M., Done, C., & Page, K. 2008, *MNRAS*, 388, 753
 Gierliński, M., Done, C., & Page, K. 2009, *MNRAS*, 392, 1106
 Godet, O., Lombardi, J. C., Antonini, F., et al. 2014, *ApJ*, 793, 105
 Graham, A. W. 2016, in *Galactic Bulges*, ed. E. Laurikainen, R. Peletier, & D. Gadotti (Berlin: Springer), 263
 Graham, A. W. 2023, *MNRAS*, 522, 3588
 Graham, A. W., & Driver, S. P. 2005, *PASA*, 22, 118
 Graham, A. W., & Sahu, N. 2023, *MNRAS*, 520, 1975
 Graham, A. W., Soria, R., Ciambur, B. C., Davis, B. L., & Swartz, D. A. 2021, *ApJ*, 923, 146
 Greene, J. E., Lancaster, L., Ting, Y.-S., et al. 2021, *ApJ*, 917, 17
 Greene, J. E., Strader, J., & Ho, L. C. 2020, *ARA&A*, 58, 257
 Grisé, F., Kaaret, P., Corbel, S., et al. 2012, *ApJ*, 745, 123
 Grupe, D., Komossa, S., & Saxton, R. 2015, *ApJL*, 803, L28
 Grupe, D., Komossa, S., & Wolsing, S. 2024, *ApJ*, 969, 98
 Guillochon, J., & Ramirez-Ruiz, E. 2015, *ApJ*, 809, 166
 Gürkan, M. A., Freitag, M., & Rasio, F. A. 2004, *ApJ*, 604, 632
 Gúrpide, A., Godet, O., Koliopanos, F., Webb, N., & Olive, J. F. 2021, *A&A*, 649, A104
 Gwyn, S. D. J. 2008, *PASP*, 120, 212
 Häberle, M., Neumayer, N., Seth, A., et al. 2024, *Natur*, 631, 285
 Hameury, J. M., & Lasota, J. P. 2020, *A&A*, 643, A171
 Hancock, S., Young, A. J., & Chainakun, P. 2023, *MNRAS*, 520, 180
 Hayasaki, K., Stone, N., & Loeb, A. 2016, *MNRAS*, 461, 3760
 Heida, M., Jonker, P. G., Torres, M. A. P., et al. 2013, *MNRAS*, 433, 681
 Heil, L. M., Vaughan, S., & Uttley, P. 2012, *MNRAS*, 422, 2620
 HI4PI Collaboration, Ben Bekhti, N., Flöer, L., et al. 2016, *A&A*, 594, A116
 Hjellming, M. S., & Webbink, R. F. 1987, *ApJ*, 318, 794
 Holoien, T. W. S., Brown, J. S., Auchettl, K., et al. 2018, *MNRAS*, 480, 5689
 Huang, X., Davis, S. W., & Jiang, Y.-f. 2024, *ApJ*, 974, 165
 Inayoshi, K., Visbal, E., & Haiman, Z. 2020, *ARA&A*, 58, 27
 Israel, G. L., Belfiore, A., Stella, L., et al. 2017, *Sci*, 355, 817
 Jetha, N. N., Hardcastle, M. J., Babul, A., et al. 2008, *MNRAS*, 384, 1344
 Jiang, J., Dausser, T., Fabian, A. C., et al. 2022, *MNRAS*, 514, 1107
 Jiang, J., Parker, M. L., Fabian, A. C., et al. 2018, *MNRAS*, 477, 3711
 Jin, C.-C., Li, D.-Y., & Jiang, N. 2025, arXiv:2501.09580
 Jordi, K., Grebel, E. K., & Ammon, K. 2006, *A&A*, 460, 339

- Kaaret, P., Feng, H., & Roberts, T. P. 2017, *ARA&A*, 55, 303
- Kalberla, P. M. W., Burton, W. B., Hartmann, D., et al. 2005, *A&A*, 440, 775
- Kalogera, V., Henninger, M., Ivanova, N., & King, A. R. 2004, *ApJL*, 603, L41
- King, A., Lasota, J.-P., & Middleton, M. 2023, *NewAR*, 96, 101672
- King, A. R., & Dehnen, W. 2005, *MNRAS*, 357, 275
- King, A. R., Kolb, U., & Szuszkiewicz, E. 1997, *ApJ*, 488, 89
- Koliopoulos, F. 2017, in XII Multifrequency Behaviour of High Energy Cosmic Sources Workshop (MULTIF2017) (Trieste: PoS), 51
- Komossa, S., & Grupe, D. 2023, *AN*, 344, e20230015
- Kovlakas, K., Zezas, A., Andrews, J. J., et al. 2020, *MNRAS*, 498, 4790
- Kraft, R. P., Burrows, D. N., & Nousek, J. A. 1991, *ApJ*, 374, 344
- Kubota, A., Ebisawa, K., Makishima, K., & Nakazawa, K. 2005, *ApJ*, 631, 1062
- Kubota, A., & Makishima, K. 2004, *ApJ*, 601, 428
- Kubota, A., Tanaka, Y., Makishima, K., et al. 1998, *PASJ*, 50, 667
- Kynoch, D., Mitchell, J. A. J., Ward, M. J., et al. 2023, *MNRAS*, 520, 2781
- Larson, R. L., Finkelstein, S. L., Kocevski, D. D., et al. 2023, *ApJL*, 953, L29
- Lasota, J.-P. 2001, *NewAR*, 45, 449
- Law, N. M., Kulkarni, S. R., Dekany, R. G., et al. 2009, *PASP*, 121, 1395
- Leitherer, C., Ekström, S., Meynet, G., et al. 2014, *ApJS*, 212, 14
- Leitherer, C., Schaerer, D., Goldader, J. D., et al. 1999, *ApJS*, 123, 3
- Li, R., Ho, L. C., Ricci, C., et al. 2022, *ApJ*, 933, 70
- Li, R., Ricci, C., Ho, L. C., et al. 2024, *ApJ*, 975, 140
- Lin, D., Irwin, J. A., Godet, O., Webb, N. A., & Barret, D. 2013, *ApJL*, 776, L10
- Lin, D., Strader, J., Carrasco, E. R., et al. 2018, *NatAs*, 2, 656
- Liu, X.-L., Dou, L.-M., Chen, J.-H., & Shen, R.-F. 2022, *ApJ*, 925, 67
- Liu, Z., Malyali, A., Krumpel, M., et al. 2023, *A&A*, 669, A75
- Lodato, G., & Rossi, E. M. 2011, *MNRAS*, 410, 359
- Lusso, E., Comastri, A., Vignali, C., et al. 2010, *A&A*, 512, A34
- MacCarone, T. J., Gallo, E., & Fender, R. 2003, *MNRAS*, 345, L19
- MacKenzie, A. D. A., Roberts, T. P., & Walton, D. J. 2023, *AN*, 344, e20230028
- Mapelli, M., Giacobbo, N., Ripamonti, E., & Spera, M. 2017, *MNRAS*, 472, 2422
- Marchesi, S., Lanzuisi, G., Civano, F., et al. 2016, *ApJ*, 830, 100
- Masetti, N., Foschini, L., Ho, L. C., et al. 2003, *A&A*, 406, L27
- Masterson, M., Kara, E., Ricci, C., et al. 2022, *ApJ*, 934, 35
- Mayer, R. J., Drinkwater, M. J., Pfeffer, J., & Baumgardt, H. 2024, *MNRAS*, 527, 4643
- Merloni, A., Fabian, A. C., & Ross, R. R. 2000, *MNRAS*, 313, 193
- Metzger, B. D. 2022, *ApJL*, 937, L12
- Metzger, B. D., & Stone, N. C. 2016, *MNRAS*, 461, 948
- Mezcua, M. 2017, *IJMPD*, 26, 1730021
- Middleton, M. J., Heil, L., Pintore, F., Walton, D. J., & Roberts, T. P. 2015, *MNRAS*, 447, 3243
- Miller, M. C., & Colbert, E. J. M. 2004, *IJMPD*, 13, 1
- Miller, M. C., & Hamilton, D. P. 2002, *MNRAS*, 330, 232
- Mineshige, S., Hirano, A., Kitamoto, S., Yamada, T. T., & Fukue, J. 1994, *ApJ*, 426, 308
- Mortlock, D. J., Warren, S. J., Venemans, B. P., et al. 2011, *Natur*, 474, 616
- Narayan, R., Sadowski, A., Soria, R., et al. 2017, *MNRAS*, 469, 2997
- NASA High Energy Astrophysics Science Archive Research Center (Heasarc), 2014 HEASoft: Unified Release of FTOOLS and XANADU, Astrophysics Source Code Library, ascl:1408.004
- Nisbet, D. M., & Best, P. N. 2016, *MNRAS*, 455, 2551
- Nixon, C. J., Coughlin, E. R., & Miles, P. R. 2021, *ApJ*, 922, 168
- O'Dell, S. L., Brissenden, R. J., Davis, W. N., et al. 2010, *Proc. SPIE*, 7803, 78030H
- Paczynski, B. 1977, *ApJ*, 216, 822
- Page, M. J., Loaring, N. S., Dwelly, T., et al. 2006, *MNRAS*, 369, 156
- Petrosian, V. 1976, *ApJL*, 210, L53
- Piconcelli, E., Jimenez-Bailón, E., Guainazzi, M., et al. 2005, *A&A*, 432, 15
- Pinto, C., Alston, W., Parker, M. L., et al. 2018, *MNRAS*, 476, 1021
- Piran, T., Svirski, G., Krolik, J., Cheng, R. M., & Shiokawa, H. 2015, *ApJ*, 806, 164
- Portegies Zwart, S. F., & McMillan, S. L. W. 2002, *ApJ*, 576, 899
- Poutanen, J., Lipunova, G., Fabrika, S., Butkevich, A. G., & Abolmasov, P. 2007, *MNRAS*, 377, 1187
- Qiu, Y., & Feng, H. 2021, *ApJ*, 922, 91
- Rau, A., Kulkarni, S. R., Law, N. M., et al. 2009, *PASP*, 121, 1334
- Remillard, R. A., & McClintock, J. E. 2006, *ARA&A*, 44, 49
- Ricarte, A., & Natarajan, P. 2018, *MNRAS*, 481, 3278
- Ricci, C., Kara, E., Loewenstein, M., et al. 2020, *ApJL*, 898, L1
- Robba, A., Pinto, C., Walton, D. J., et al. 2021, *A&A*, 652, A118
- Roth, N., Kasen, D., Guillochon, J., & Ramirez-Ruiz, E. 2016, *ApJ*, 827, 3
- Sacchi, A., Risaliti, G., & Miniutti, G. 2023, *A&A*, 671, A33
- Saxton, R., Komossa, S., Auchettl, K., & Jonker, P. G. 2020, *SSRv*, 216, 85
- Schellenberger, G., Vrtilik, J. M., David, L., et al. 2017, *ApJ*, 845, 84
- Schlafly, E. F., & Finkbeiner, D. P. 2011, *ApJ*, 737, 103
- Schlegel, D. J., Finkbeiner, D. P., & Davis, M. 1998, *ApJ*, 500, 525
- Seepaul, B. S., Pacucci, F., & Narayan, R. 2022, *MNRAS*, 515, 2110
- Shakura, N. I., & Sunyaev, R. A. 1973, *A&A*, 24, 337
- Shimura, T., & Takahara, F. 1995, *ApJ*, 445, 780
- Shiokawa, H., Krolik, J. H., Cheng, R. M., Piran, T., & Noble, S. C. 2015, *ApJ*, 804, 85
- Siemiginowska, A., Burke, D., Günther, H. M., et al. 2024, *ApJS*, 274, 43
- Singal, J., Mutchnick, S., & Petrosian, V. 2022, *ApJ*, 932, 111
- Soria, R., Hakala, P. J., Hau, G. K. T., Gladstone, J. C., & Kong, A. K. H. 2012, *MNRAS*, 420, 3599
- Soria, R., Musaeva, A., Wu, K., et al. 2017, *MNRAS*, 469, 886
- Steinberg, E., & Stone, N. C. 2024, *Natur*, 625, 463
- Steiner, J. F., Narayan, R., McClintock, J. E., & Ebisawa, K. 2009, *PASP*, 121, 1279
- Stone, N. C., & Metzger, B. D. 2016, *MNRAS*, 455, 859
- Sutton, A. D., Done, C., & Roberts, T. P. 2014, *MNRAS*, 444, 2415
- Sutton, A. D., Roberts, T. P., Gladstone, J. C., & Walton, D. J. 2015, *MNRAS*, 450, 787
- Sutton, A. D., Roberts, T. P., & Middleton, M. J. 2013, *MNRAS*, 435, 1758
- Sutton, A. D., Roberts, T. P., Walton, D. J., Gladstone, J. C., & Scott, A. E. 2012, *MNRAS*, 423, 1154
- Sutton, A. D., Swartz, D. A., Roberts, T. P., et al. 2017, *ApJ*, 836, 48
- Tang, V. L., Madau, P., Bortolas, E., et al. 2024, *ApJ*, 963, 146
- Terashima, Y., Kamizasa, N., Awaki, H., Kubota, A., & Ueda, Y. 2012, *ApJ*, 752, 154
- Thomsen, L. L., Kwan, T. M., Dai, L., et al. 2022, *ApJL*, 937, L28
- Thornton, C. E., Barth, A. J., Ho, L. C., Rutledge, R. E., & Greene, J. E. 2008, *ApJ*, 686, 892
- Tody, D. 1986, *Proc. SPIE*, 627, 733
- Tody, D. 1993, in ASP Conf. Ser. 52, Astronomical Data Analysis Software and Systems II, ed. R. J. Hanisch, R. J. V. Brissenden, & J. Barnes (San Francisco, CA: ASP), 173
- Tranin, H., Godet, O., Webb, N., & Primorac, D. 2022, *A&A*, 657, A138
- Tranin, H., Webb, N., Godet, O., & Quintin, E. 2024, *A&A*, 681, A16
- van der Helm, E., Portegies Zwart, S., & Pols, O. 2016, *MNRAS*, 455, 462
- van Velzen, S., Stone, N. C., Metzger, B. D., et al. 2019, *ApJ*, 878, 82
- Vaughan, S., Edelson, R., Warwick, R. S., & Uttley, P. 2003, *MNRAS*, 345, 1271
- Vierdayanti, K., Watarai, K.-Y., & Mineshige, S. 2008, *PASJ*, 60, 653
- Volonteri, M., Habouzit, M., & Colpi, M. 2021, *NatRP*, 3, 732
- Volonteri, M., Lodato, G., & Natarajan, P. 2008, *MNRAS*, 383, 1079
- Walton, D. J., Bachetti, M., Kosec, P., et al. 2024, arXiv:2409.12241
- Walton, D. J., Fürst, F., Harrison, F. A., et al. 2018a, *MNRAS*, 473, 4360
- Walton, D. J., Fürst, F., Heida, M., et al. 2018b, *ApJ*, 856, 128
- Walton, D. J., Pinto, C., Nowak, M., et al. 2020, *MNRAS*, 494, 6012
- Wang, F., Yang, J., Fan, X., et al. 2021, *ApJL*, 907, L1
- Watarai, K.-y., Fukue, J., Takeuchi, M., & Mineshige, S. 2000, *PASJ*, 52, 133
- Webb, N. A., Coriat, M., Traulsen, I., et al. 2020, *A&A*, 641, A136
- Webbink, R. F. 1985, in *Interacting Binary Stars*, ed. J. E. Pringle & R. A. Wade (Cambridge: Cambridge Univ. Press), 39
- Wevers, T., Pasham, D. R., van Velzen, S., et al. 2019, *MNRAS*, 488, 4816
- Willingale, R., Starling, R. L. C., Beardmore, A. P., Tanvir, N. R., & O'Brien, P. T. 2013, *MNRAS*, 431, 394
- Wilms, J., Allen, A., & McCray, R. 2000, *ApJ*, 542, 914
- Wright, E. L. 2006, *PASP*, 118, 1711
- Xu, Y., Pinto, C., Rogantini, D., et al. 2024, *A&A*, 687, A179
- Yang, J., Wang, F., Fan, X., et al. 2020, *ApJL*, 897, L14
- Zolotukhin, I., Webb, N. A., Godet, O., Bachetti, M., & Barret, D. 2016, *ApJ*, 817, 88